

MCHex: Marching Cubes Based Adaptive Hexahedral Mesh Generation with Guaranteed Positive Jacobian

Hua Tong
Carnegie Mellon University
huat2@andrew.cmu.edu

Yongjie Jessica Zhang
Carnegie Mellon University
jessicaz@andrew.cmu.edu

Abstract

Grid-based methods remain the most reliable approach for automatic hexahedral (hex) meshing, but struggle with boundary fidelity and mesh quality. Conventional pipelines initialize by removing outside elements (RO), yielding poor axis-aligned approximations of arbitrary input geometries. Subsequent projection is heuristic, lacking guarantees on boundary fidelity or mesh quality. This paper introduces a fundamental reformulation of boundary and mesh quality handling in grid-based hex meshing. Instead of RO, each grid cell is processed using Marching Cubes to extract the zero-isosurface relative to the input geometry. The key insight is that the cutted cell form 3-regular graphs, which, after midpoint subdivision, guarantee all-hex elements with positive Jacobian. The MCHex method offers three advantages: (1) theoretical guarantee of positive Jacobian for all elements, (2) faster boundary convergence than RO, and non-heuristic with well-bounded time complexity, (3) generation of manifold surfaces for arbitrary geometries, intrinsically resolving topology ambiguities and providing boundary pillowing. Extensive evaluation on Thingi10K dataset confirms these advantages by comparing MCHex to RO within same time budget. Moreover, MCHex ensures all-positive scaled Jacobian and high-quality boundary fitting, where existing software fail to achieve simultaneously. MCHex can be seamlessly integrated with optimization-based boundary smoothing and simplification algorithms to form a complete pipeline.

1 Introduction

Hex mesh generation has long been regarded as a fundamental yet challenging problem in computational geometry and scientific computing. Hex meshes are highly desirable in finite element analysis (FEA) and isogeometric analysis (54) due to their superior numerical properties compared to tetrahedral meshes,

offering better convergence rates, lower computational cost, and higher accuracy for many physical simulations (4, 10, 44, 45). Despite decades of research, automatically generating high-quality, all-hex meshes that conform to complex geometries while maintaining good mesh quality remains an open problem (37, 5, 32, 40, 41, 47). A wide spectrum of approaches has been explored, ranging from advancing front (7), dual approach (48), domain decomposition (1), grid-based (38), polycube maps (16, 46) to frame fields (31); however, most of these methods either require significant user intervention, lack robustness on general inputs, no quality guarantees, or involve long computation time (34).

Among various mesh generation strategies, the grid-based method has become the most reliable approach and the only one widely adopted in industrial practice (20, 11). The algorithm typically starts by adaptively refining a Cartesian grid until a specified criterion is met. Commonly used criteria include error-sensitive functions (48, 50, 51, 19), normal similarity (21), local thickness (28, 27, 35, 42), and surface approximation accuracy (15, 33).

After refinement, hanging nodes in the grids are eliminated by replacing cells with transition templates that locally restore mesh conformity. Existing methods can be classified into primal and dual approaches. Primal methods directly incorporate hanging nodes into the output hex mesh. For 3-refinement schemes, the first method was introduced by (39), but it could not handle concave regions effectively, leading to excessive refinement. Subsequent works improved this by developing templates for concave edges (21, 13). In contrast, 2-refinement templates, though more challenging to implement, can mesh both convex and concave regions with fewer elements (12, 51, 33).

Dual methods, which are exclusively applied to 2-refinement schemes, modify the input grids so that the dual mesh consists entirely of hex elements. These methods represent a significant direction for

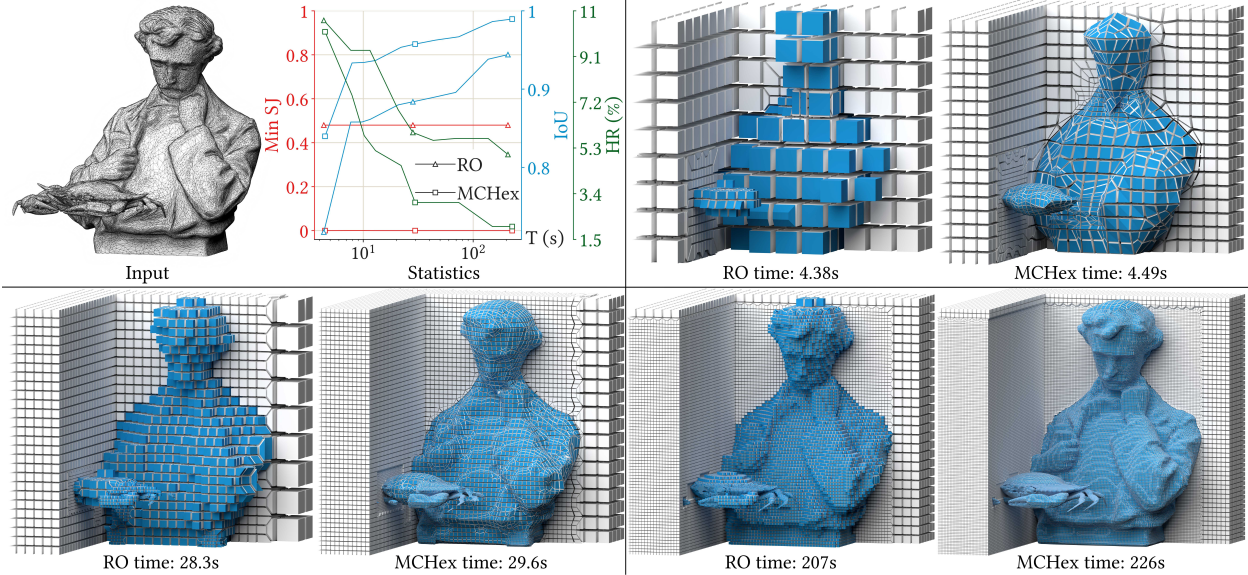


Figure 1: Constructing an adaptive hexahedral tessellation to fit an input triangle boundary is a key challenge in grid-based methods. The conventional method first removes outside elements (RO) and then projects the axis-aligned boundary onto the input triangle boundary, which has no guarantee on improving the initial Intersection over Union (IoU) and Hausdorff distance ratio (HR, w.r.t bounding box diagonal). The proposed MCHex approach replaces RO with a Marching Cubes method MCHex. Given the same computational budget (benchmarked using an identical precomputed Signed Distance Field, which dominates the runtime), MCHex provides better boundary approximation (higher IoU and lower HR) while guaranteeing a lower, yet still positive, minimum scaled Jacobian (> 0 vs. RO’s ≥ 0.48).

reducing mesh size. Their primary advantage over primal methods is that transition cells do not propagate across three layers. The development of these methods has been a trajectory of relaxing constraints. The first proposed method required strong balancing and octree pairing (28), a requirement retained in two later pipelines (15, 42). Subsequent studies optimized the transition templates to reduce element counts (19). A significant advancement was made by (27), who introduced rotation-symmetric templates to reduce irregular valence and expanded the template set to relax the strong balancing condition to weak balancing and greatly reduced the element count. The most element-efficient method to date further relaxed octree pairing to generalized pairing by using linear programming to ensure an even number of same-density cells in all three directions (35). It is noteworthy, however, that the reduction in element count does not come without cost. It is achieved at the expense of lowering the upper bound on element quality. For example, based on the authors’ experiments, the original 3-refinement templates (39) yield a minimum scaled Jacobian of 0.48 without any optimization, while more recent methods employing weak balancing and generalized pairing produce minimum scaled Jacobians on the order of 10^{-3} (27, 35).

Although optimization techniques can mitigate these issues, the increasingly complex topological connections inherently constrain the upper bound of mesh quality that can be achieved through warping points.

The final step in the pipeline involves boundary projection. Due to the axis-aligned nature of grid-based meshing, boundary vertices must be projected onto the target geometry to accurately approximate the input surface. Early methods projected vertices directly without preprocessing, often resulting in poor element quality at the boundary. This degradation stems from a well-documented issue: when multiple faces of a single hex element lie on the boundary, projecting their vertices independently onto the target surface can induce significant distortion. The combination of padding or pillowing techniques addressed this issue by ensuring that each boundary element has only one face to be projected (30). This has since become a standard step in nearly all grid-based meshing pipelines. However, the topological variability of surface vertex stars, ideally homeomorphic to a disk but sometimes more complex, requires careful handling, often involving single or multiple pillowed points depending on the configuration (21, 15, 42). Following pillowing, all methods apply optimization or smoothing techniques to project the

pillowed vertices onto the target surface while optimizing mesh quality. Notably, while all preceding steps in the pipeline have deterministic time complexity with guaranteed mesh quality bounds, the final projection step remains largely heuristic. In quadrilateral (quad) and tetrahedral mesh generation, methods already exist that guarantee both perfect boundary conformity and superior angle range, while preserving sharp features (22, 23, 24). Although some optimization methods in hex meshing ensure a positive Jacobian (25), such guarantees are of limited practical value, as they do not provide a lower bound on the improvement of geometric fidelity between the initial axis-aligned boundary and the final optimized boundary. The main observation by the authors is that this fundamental limitation is one of the key reasons for the slow progress in hex mesh generation over the past decade. In contrast, tetrahedral mesh generation, backed by rigorous theoretical guarantees from constrained Delaunay tetrahedralization, both in terms of element quality and boundary preservation, has seen wider adoption in commercial applications.

In this paper, the authors introduce MCHex, a novel hex meshing approach based on the Marching Cubes (MC) algorithm. Unlike conventional methods that simply remove outside elements (RO), resulting in axis-aligned boundaries and slow geometric convergence, MCHex directly uses the MC isosurface as the mesh boundary, enabling faster convergence under same computation time while rigorously ensuring that all hex elements maintain positive Jacobians. This is illustrated in the 2024 International Meshing Roundtable Meshing Contest model in Figure 1. After obtaining the spatial tessellation from the grid, instead of removing elements outside the input geometry as in conventional approaches, the new technique computes the Signed Distance Field (SDF) value relative to the input geometry for all points. Each cell is then processed using MC to extract the zero-isosurface. It is observed that the reconstructed isosurface consistently partitions each cell into two or more polyhedra, whose graph structures are necessarily 3-regular. Applying midpoint subdivision to a 3-regular graph yields a Closure-finite Weak topology complex (CW complex) composed entirely of hexes. Each resulting hex element shares at most one face with the isosurface. Also, the Jacobian of each hex element is theoretically guaranteed to remain positive. As a result, the MCHex method offers the following three key advantages:

1. The Jacobian of every hex element is guaranteed to be positive with rigorous proof.

2. It achieves faster convergence toward the input geometry compared to previous grid-based hex meshing pipelines that rely on removing outside elements, and the algorithm is non-heuristic, with well-bounded time complexity linear to the multiplication of the size of input triangle faces and the size of grids.
3. MC ensures the generation of a manifold surface with intrinsically pillowed boundary, and a local refinement lookup table resolves MC topology ambiguities within each cell, ensuring correct topology.

The MCHex method has been tested on all the models in Thingi10K. This includes a large-scale comparison with the prior RO method, analyzing time complexity, minimum scaled Jacobian, Intersection over Union (IoU), and Hausdorff distance ratio (HR) normalized by the bounding box diagonal. Furthermore, a comparative analysis is presented on models where state-of-the-art methods (20, 15) fail to maintain both positive scaled Jacobian and accurate boundary approximation.

The remainder of the paper is organized as follows. Section 2 presents rationale of the MCHex method. Section 3 provides an overview to the proposed algorithm. Section 4 outlines the beneficial properties of 3-regular graphs that guarantee the generation of all-hex meshes following midpoint subdivision. Section 5 provides a proof that all hexes have positive Jacobian. Section 6 provides an extensive evaluation on the Thingi10K dataset. Finally, Section 7 summarizes the key contributions and suggests potential future research directions. For full reproducibility, the reference implementation is included in the supplementary materials and will be made publicly available on GitHub after the paper is accepted.

2 Rationale

The foundational concept for the MCHex approach is inspired by work on quad meshing without cleanup operations (36), as summarized in Figure 2. The left three panels illustrate the RO method commonly employed in previous grid-based hex or quad meshing pipelines. This method exhibits two significant limitations: (1) the resulting boundary is axis-aligned, creating substantial deviation from the input geometry, and (2) as a consequence of this poor initial approximation, subsequent optimization induces severe distortion in boundary elements, making them highly susceptible to inversion. To mitigate such inversions, additional pillowing of boundary elements is typically

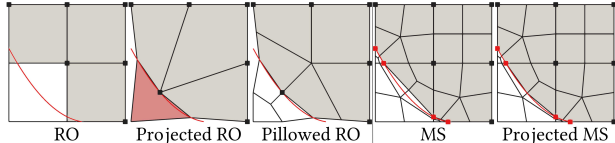


Figure 2: Adapting a uniform grid (black) to an input curve (red) using two methods. The RO method begins with an axis-aligned boundary that is a poor approximation. Projection causes significant distortion and an inverted element (red), necessitating a pillowing fix. The MS method generates an initial mesh whose boundary is already a close fit to the geometry. Projection requires only slight adjustments to edge midpoints.

required. In contrast, the right two panels demonstrate the Marching Squares (MS)-based approach. It introduces the concept of midpoint subdivision for boundary-cut squares to generate all-quad elements. Notably, even before projection, the mesh boundary derived from the red intersection points closely approximates the input geometry. Furthermore, this construction guarantees positive Jacobian values for all elements. The close initial fit ensures that subsequent projection introduces minimal distortion to boundary elements, significantly reducing the occurrence of inversion and the need for corrective optimization. The issue of poorly shaped elements was addressed by implementing a vertex repelling strategy: when intersection points approach too closely to grid points, the grid points are repelled to maintain reasonable edge ratios. Thanks to the direct geometric interpretation of quad Jacobian as the sine value of the interior angle, this procedure theoretically guarantees maintained positive Jacobian quality. In addition, extra templates were introduced to preserve sharp geometric features.

However, extending this approach to three dimensions introduces substantial challenges. The same authors proposed a three-dimensional hex meshing variant (2), but the demonstrated results were three simple geometries: a sphere, a doll, and a cylinder, without providing any guarantees on mesh quality. Furthermore, the method was restricted to uniform grids, unlike the adaptive grid framework employed in the two-dimensional case. Here, three primary difficulties emerge. First, the original formulation failed to recognize that the method’s essence lies in combining MC with midpoint subdivision. Instead, the authors simplified the problem to five basic cases of planar-cube intersections. In practice, the topological configurations of input geometry within a cube are considerably more complex, and intersection points on cutting surfaces with more than three vertices

are frequently non-coplanar. Second, while midpoint subdivision of an arbitrary n -gon in two dimensions invariably produces n quads, the three-dimensional case imposes stricter constraints. As discussed later in Section 4, only polyhedra with 3-regular graph connectivity containing n vertices are bounded to yield n hexes after midpoint subdivision. Third, the geometric interpretation of Jacobian quality becomes significantly more complex. In two-dimensions, the Jacobian is related to the sine of the interior angles; in three-dimensions, it corresponds to the signed volume of the tetrahedron formed by a vertex’s three edges. This geometric complexity, combined with the diverse configurations in adaptive grids, makes establishing rigorous quality guarantees significantly more difficult. This paper aims to provide a comprehensive and rigorous treatment of these three challenges, presenting theoretical foundations and practical solutions for robust three-dimensional hex meshing.

3 Algorithm Overview

Of particular interest in the storage of three-dimensional geometry is a closed pure two-dimensional simplicial complex T_{geom} . According to the Jordan-Brouwer separation theorem (18), T_{geom} partitions \mathbb{R}^3 into two connected components: a bounded internal region $\text{Int}(T_{\text{geom}})$ and an unbounded external region $\mathbb{R}^3 \setminus \text{Int}(T_{\text{geom}})$. To address computer memory constraints, an axis-aligned bounding box (AABB) T_{AABB} is introduced, which also partitions \mathbb{R}^3 into a bounded internal region $\text{Int}(T_{\text{AABB}})$ and an unbounded external region $\mathbb{R}^3 \setminus \text{Int}(T_{\text{AABB}})$, with the condition that $\text{Int}(T_{\text{geom}}) \subset \text{Int}(T_{\text{AABB}})$.

Let $M \subset \mathbb{R}^3$ be a solid region, the hex mesh $H_M = (V, E, Q, H)$ is a CW-complex (18) of hex elements H that decomposes M . V, E, Q and H represent the vertices, the edges, the quad faces, and the hex elements, respectively. The boundary ∂H consists of those faces in Q belonging to only one hex element, along with their constituent edges and vertices. Hex elements in H that are not part of ∂H are referred to as internal elements. The domain $\text{Int}(T_{\text{AABB}})$ is tessellated into hexes $H_{\text{Int}(T_{\text{AABB}})}$. Given the hex mesh $H_{\text{Int}(T_{\text{AABB}})}$, the algorithm extracts $H_{\text{Int}(T_{\text{geom}})}$ and $H_{\text{Int}(T_{\text{AABB}}) \setminus \text{Int}(T_{\text{geom}})}$, both of which are bounded to satisfy the following properties: positive Jacobian, accurate boundary (i.e., correct topology, high IoU, and low HR), and C^0 -conformity along their shared boundary. Specifically, “adaptivity” requires the mesh to be denser near high-frequency features and coarser in smoother

regions to save elements. “ C^0 -conformity” means two piecewise linear meshes are topologically and geometrically consistent across their common quad boundary faces. In detail, there exists a bijection $\phi : \partial H_{\text{Int}(T_{\text{geom}})} \rightarrow \partial H_{\text{Int}(T_{\text{AABB}}) \setminus \text{Int}(T_{\text{geom}})}$ such that for each quad face $q(V_q, E_q) \in \partial H_{\text{Int}(T_{\text{geom}})}$, face $\phi(q) \in \partial H_{\text{Int}(T_{\text{AABB}}) \setminus \text{Int}(T_{\text{geom}})}$ satisfies $\phi(v) = v$ and $\phi(e) = e$ for $v \in V_q$ and $e \in E_q$.

Algorithm 1: Hex meshing of an input geometry

Input: Closed pure 2D simplicial complex $T_{\text{geom}}, T_{\text{AABB}}$

Output: Hex meshes $H_{\text{Int}(T_{\text{geom}})}$ and $H_{\text{Int}(T_{\text{AABB}}) \setminus \text{Int}(T_{\text{geom}})}$

Initialize grids with 3-refinement strategy;

for each cell do

while *feature-sensitive error* > *user threshold* **do**

 Recursively subdivide cell into 27 child cells;

Apply standard 3-refinement templates to get adaptive hex mesh $H_{\text{Int}(T_{\text{AABB}})}$;

Compute SDF values for every grid point in $H_{\text{Int}(T_{\text{AABB}})}$;

for each cell in $H_{\text{Int}(T_{\text{AABB}})}$ **do**

if *eight SDF values have different signs* **then**

 Construct isosurface dividing the cell into inside/outside 3-regular graphs using MC method;

for each 3-regular graph do

 Apply midpoint subdivision;

 Generate all-hex mesh: $H_{\text{Int}(T_{\text{geom}})}$ (inside geometry) and $H_{\text{Int}(T_{\text{AABB}}) \setminus \text{Int}(T_{\text{geom}})}$ (outside geometry);

Warp volume center points to ensure positive Jacobian;

return $H_{\text{Int}(T_{\text{geom}})}, H_{\text{Int}(T_{\text{AABB}}) \setminus \text{Int}(T_{\text{geom}})}$;

The complete pipeline is summarized in Algorithm 1. The process begins by initializing grids using a 3-refinement strategy. Each cell is recursively subdivided into twenty-seven cells until the feature-sensitive error function for every cell falls below a user-defined threshold. The original feature-sensitive error function, defined as $\sum_{i=1}^{27} \frac{|f^{j+1}(\mathbf{x}_i) - f^j(\mathbf{x}_i)|}{|\nabla f^j(\mathbf{x}_i)|}$ (49), where \mathbf{x}_i are position vectors at corners of eight cells after 2-refinement, j is the grid level, has been modified to $\max_{i=1}^{64} \frac{|f^{j+1}(\mathbf{x}_i) - f^j(\mathbf{x}_i)|}{|\nabla f^j(\mathbf{x}_i)|}$, where \mathbf{x}_i are position vectors at corners of twenty-seven cells after 3-refinement, j is the grid level, in order to fit to the 3-

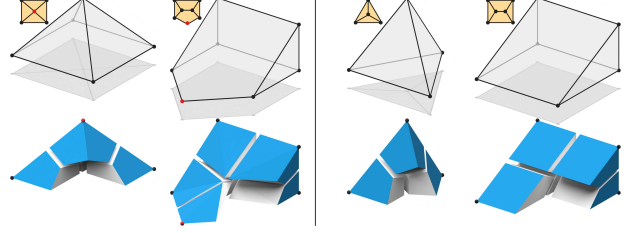


Figure 3: The left two polyhedra are non-3-regular, with violated vertices marked by red dots; the right two polyhedra are 3-regular. The top row illustrates the two-dimensional CW complexes (transparent grey) with 1-skeleton (yellow), while the bottom row shows the resulting three-dimensional volumetric meshes after applying midpoint subdivision. One element is removed in each example to show the interior.

refinement scheme (39) and prioritize the subdivision of cells with extreme values. Subsequently, the standard 3-refinement templates are applied to eliminate hanging nodes, resulting in an adaptive hex mesh, $H_{\text{Int}(T_{\text{AABB}})}$, where the SDF value is computed for every grid point. Next, the MC method is employed within each cell. Since the SDF values at all eight grids are known, an isosurface can be constructed for each cell, dividing the cell into an inside and an outside 3-regular graph. The final step involves subdividing every 3-regular graph using the midpoint subdivision. This subdivision produces an all-hex mesh that partitions the domain into $H_{\text{Int}(T_{\text{geom}})}$ (inside the geometry) and $H_{\text{Int}(T_{\text{AABB}}) \setminus \text{Int}(T_{\text{geom}})}$ (outside the geometry), separated by the reconstructed isosurface. To guarantee that all hexes have a positive Jacobian, some volume centroids are warped based on theoretically-derived positions which will be explained later in Section 5.

4 Properties of 3-regular graph

This section begins by establishing the definitions of a k -regular graph, a k -regular polyhedron, and the midpoint subdivision operation. It then provides a formal proof that the midpoint subdivision of a polyhedron induces all-hex elements if and only if the polyhedron is 3-regular. The necessity of this condition is also proved by showing that any 3-regular polyhedron satisfy the Global Necessary Condition for hex meshing proposed in (26).

Definition 4.1 (k -regular graph). *A k -regular graph is an undirected graph $G = (V, E)$ where every vertex $v \in V$ is incident to k edges or has k neighboring vertices.*

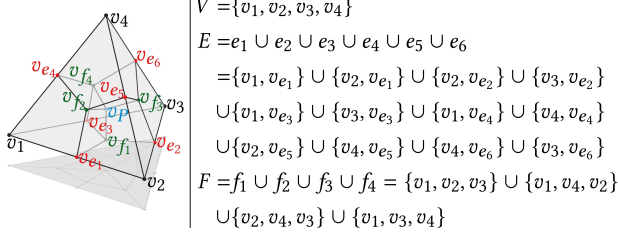


Figure 4: An example of midpoint subdivision converting a tetrahedral boundary $P = (V, E, F)$ into mesh $P' = (V', E', F', C')$ composed of four hex elements, illustrating Theorem 4.1.

Definition 4.2 (k -regular polyhedron). $P = (V, E, F)$ is a closed pure two-dimensional CW complex, where each face in F is attached to a cycle in the 1-skeleton of P . The 1-skeleton, which consists of the vertices V and edges E , forms the underlying graph structure of the complex. If the underlying graph (V, E) is a k -regular graph (where each vertex has k neighboring vertices), then P is a k -regular polyhedron.

In the first row of Figure 3, the left two are non-3-regular polyhedra, while the right two are 3-regular polyhedra. Their 1-skeletons are shown at the left-top corner of each polyhedron in yellow.

Definition 4.3 (midpoint subdivision). The midpoint subdivision of a closed pure two-dimensional CW complex $P = (V, E, F)$ induces a pure three-dimensional CW complex $P' = (V', E', F', C')$ as follows: For each edge $e(V_e) \in E$, insert edge midpoint $v_e = \frac{1}{|V_e|} \sum_{v \in V_e} v$. For each face $f(V_f, E_f) \in F$, insert face midpoint $v_f = \frac{1}{|V_f|} \sum_{v \in V_f} v$, then for each edge $e \in E_f$, connect edge midpoint v_e to v_f . Insert volume center $v_P = \frac{1}{|V|} \sum_{v \in V} v$. For each face $f \in F$, connect the face midpoint v_f to v_P . The resulting structure is induced to form $P' = (V', E', F', C')$.

The focus of this definition is the topological changes to the graph connectivity and the cellular complex by the subdivision. Geometrically, the positions of newly inserted points are usually midpoints (e.g., centroids), as shown in the second row of Figure 3 and in Figure 4. However, as will be shown in Section 5, deviating from geometric centroid positions is sometimes necessary to preserve positive Jacobian determinant.

Theorem 4.1. Let $P = (V, E, F)$ be a closed pure two-dimensional CW complex (e.g., Figure 4), and $P' = (V', E', F', C')$ be the pure three-dimensional CW complex induced by applying midpoint subdivision to P . Then every element $c \in C'$ is a hex if and only if P is a 3-regular polyhedron.

Proof. As shown in Figure 4, elements in the complex P' is formed by constructing a unique element, denoted c_v , around each vertex $v \in V$ of the original complex P . Let $\text{val}(v)$ be the face valence of vertex v . The number of vertices, edges and faces of element c_v are checked as follows.

The vertices of element c_v , denoted V_v , are composed of: the original vertex v ; a new vertex v_P at the volume centroid of P ; the set of new vertices $\{v_{f_i}\}_{i=1}^{\text{val}(v)}$ at the centroids of faces adjacent to v ; and the set of new vertices $\{v_{e_i}\}_{i=1}^{\text{val}(v)}$ at the midpoints of edges incident to v . Therefore, the total number of vertices in c_v is $|V_v| = 1$ (original vertex v) + 1 (volume center) + $\text{val}(v)$ (face centers) + $\text{val}(v)$ (edge midpoints) = $2\text{val}(v) + 2$.

The edges of element c_v , denoted E_v , are composed of: edges connecting the original vertex v to the midpoints of its incident edges $\{v_{e_i}\}_{i=1}^{\text{val}(v)}$; edges connecting the volume centroid v_P to the centroids of the adjacent faces $\{v_{f_i}\}_{i=1}^{\text{val}(v)}$; edges connecting each face centroid v_{f_i} to the midpoints of its two edges v_{e_i} and $v_{e_{i+1}}$ (with indices taken modulo $\text{val}(v)$). Therefore, the total number of edges in c_v is $|E_v| = \text{val}(v) + \text{val}(v) + 2\text{val}(v) = 4\text{val}(v)$.

The faces of element c_v , denoted F_v , are composed of two categories: quads formed by the original vertex v , a face centroid v_{f_i} , and two edge midpoints v_{e_i} and $v_{e_{i+1}}$; quads formed by the volume centroid v_P , an edge midpoint $v_{e_{i+1}}$, and two face centroids v_{f_i} and $v_{f_{i+1}}$ adjacent to that edge. Each category has $\text{val}(v)$ faces. Therefore, the total number of faces in c_v is $|F_v| = 2\text{val}(v)$.

To approve the if and only if statement, it is needed to approve both the sufficiency condition (\Rightarrow) and the necessary condition (\Leftarrow).

(\Rightarrow) Assume that every element $c \in C'$ is a hex. This means that for any given vertex $v \in V$, the corresponding element c_v is a hex. By definition, a hex is an element with 8 vertices. Thus, for any c_v , $|V_v| = 8$. Using the established vertex count formula, it follows that $2\text{val}(v) + 2 = 8$, therefore $\text{val}(v) = 3$. Since this condition must hold for every vertex $v \in V$, the polyhedron P must be 3-regular.

(\Leftarrow) Assume that P is a 3-regular polyhedron. This means that for every vertex $v \in V$, its valence is $\text{val}(v) = 3$. Therefore, for element c_v , $|V_v| = 2\text{val}(v) + 2 = 2(3) + 2 = 8$, $|E_v| = 4\text{val}(v) = 4(3) = 12$, $|F_v| = 2\text{val}(v) = 2(3) = 6$. An element with 8 vertices, 12 edges, and 6 quad faces must be a hex. Therefore, if P is 3-regular, every element c_v is a hex.

With both the sufficiency and necessary conditions hold, it is approved that every element $c \in C'$ is a hex if and only if P is a 3-regular polyhedron.

□

As an extension, it holds that the three-dimensional CW complex $P' = (V', E', F', C')$ induced by 3-regular two-dimensional CW complex $P = (V, E, F)$ satisfy the hex-meshing Global Necessary Condition (26). This equation establishes a global constraint that the resulting hex mesh in P' must satisfy:

$$\begin{aligned} & \sum_{v \in \partial V'} (4 - \text{val}(v)) + \sum_{v \in \dot{V}'} (8 - \text{val}(v)) \\ &= \sum_{e \in \partial E'} \text{idx}(e) + \sum_{e \in \dot{E}'} \text{idx}(e), \end{aligned} \quad (1)$$

where $\partial V'$ and \dot{V}' denote the boundary and internal vertices of P' , and $\partial E'$ and \dot{E}' denote the boundary and internal edges of P' . Additionally, $\text{val}(v), \text{val}(e) \in \mathbb{N}_{\geq 1}$ are the number of adjacent elements surrounding a vertex v and an edge e , respectively, and

$$\text{idx}(e) = \begin{cases} 4 - 2\text{val}(e), & \text{for } e \in \partial E' \\ 8 - 2\text{val}(e), & \text{for } e \in \dot{E}'. \end{cases} \quad (2)$$

The vertex set V' in P' is formed from the original vertex set V by adding all edge midpoints, face centers, and the volume centroid, yielding $\partial V' = V \cup \{v_e\}_{e \in E} \cup \{v_f\}_{f \in F}$. It holds that $\text{val}_{v \in V}(v) = 1$ (each corner point of V belongs to only one element in P'), $\text{val}_{v \in \{v_e\}_{e \in E}}(v) = 2$ (each edge midpoint is shared by two elements in P'), $\text{val}_{v \in \{v_f\}_{f \in F}}(v) = |V_f|$ (each face centroid is shared by $|V_f|$ elements in P'), and $\text{val}_{v \in \dot{V}'}(v) = \text{val}(v_P) = |V|$ (the volume center is shared by $|V|$ elements in P'), where $|V|$ is the number of vertices in P , and $|V_f|$ is the number of vertices in face f (see the example in Figure 4). Therefore, the left-hand side of Equation 1 can be simplified as:

$$(4 - 1)|V| + (4 - 2)|E| + \sum_{f \in F} (4 - |V_f|) + (8 - |V|), \quad (3)$$

where $|E|$ is the number of edges in polyhedron P .

The edge set E' in P' is formed from the original edge set E by adding face-center to edge-midpoint edges and face-center to volume-centroid edges, yielding $\partial E' = E \cup \{v_{e_f}, v_f\}_{f \in F, e_f \in E_f}$. It holds that $\text{val}(e) = 1$ for $e \in E$, so $\text{idx}_{e \in E}(e) = 2$; $\text{val}(e) = 1$ for $e \in \{v_{e_f}, v_f\}_{f \in F, e_f \in E_f}$, so $\text{idx}_{e \in \{v_{e_f}, v_f\}_{f \in F, e_f \in E_f}}(e) = 0$; and $\text{val}(e) = |V_f|$ for $e \in \{v_P, v_f\}_{f \in F}$, so $\text{idx}_{e \in \dot{E}'}(e) = \text{idx}_{e \in \{v_P, v_f\}_{f \in F}}(e) = 8 - 2|V_f|$. As a result,

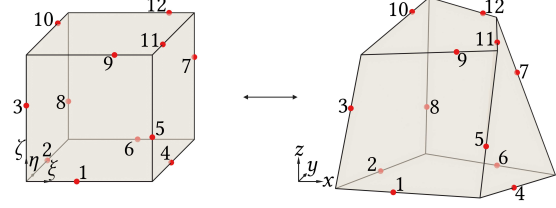


Figure 5: Coordinate transformation of a hex element from its local parametric space (left) to the global physical space (right). Twelve red points, numbered 1 through 12, represent the intersection points at twelve edges.

the right-hand side of the Global Necessary Condition can be simplified as:

$$2(2|E|) + \sum_{f \in F} (8 - 2|V_f|). \quad (4)$$

Note that each edge in P is split into two edges in P' . In addition, Euler's formula holds that:

$$|V| - |E| + |F| = 2, \quad (5)$$

where $|F|$ is the number of faces in P .

Furthermore, by Definition 4.1, each vertex in a 3-regular graph is incident to exactly 3 half-edges. Since each edge comprises 2 half-edges, the total number of edges is given by the handshaking lemma $|E| = 1.5|V|$. Substituting Equation 3 and Equation 4 into Equation 1, and considering Equation 5 and $|E| = 1.5|V|$, it is eventually obtained that:

$$\sum_{f \in F} |V_f| = 3|V|. \quad (6)$$

This identity follows from the combinatorial properties of 3-regular polyhedron. Since each edge is incident to two faces and each face with $|V_f|$ vertices also has $|V_f|$ edges, therefore $\sum_{f \in F} |V_f| = 2|E| = 3|V|$, which completes the proof.

5 Positive Jacobian Proof

This section begins by defining the Jacobian determinant as a key measure of element quality. The MC method (9) is then applied to reconstruct the isosurface within each cell $h \in H_{\text{Int}(T_{\text{AABB}})}$ where the SDF values at its eight grids exhibit sign changes. It is demonstrated that the cells intersected by the isosurface are all 3-regular, making them hex meshable via midpoint subdivision. Among a total of thirty-one topological cases in a marching cube, fourteen templates guaranteed to generate positive Jacobian hexes under midpoint subdivision are listed and

proven. The other seventeen cases for which a guarantee failed to be established are transferred into the fourteen templates using local refinement. Local refinement is introduced to transform these failed cases into the fourteen cases with proof certificates. Additionally, since the cell intersected by the isosurface can be transition cells or non-cubic cells, the positive Jacobian proofs are therefore given to not only the cubic cell, but all possible deformed hex elements. As a proof of concept, complete proofs for the vanilla 3-refinement templates presented in (39, 48) are provided. Based on the experience, it is highly feasible to extend the proofs to element-saving 3-refinement templates (21) and 2-refinement templates (51, 33) as well. Such tasks are left for future work.

As shown in Figure 5, the finite element discretization of complex geometries employs a coordinate transformation to map hex elements with regular geometry in local coordinates (ξ, η, ζ) (or called parametric domain in the left panel) to distorted hex elements in global Cartesian coordinates (x, y, z) (or called physical domain in the right panel). This transformation is typically implemented using an interpolation scheme based on nodal shape functions, written as:

$$\begin{bmatrix} x \\ y \\ z \end{bmatrix} = \mathbf{X} \cdot \mathbf{N}(\xi, \eta, \zeta), \quad (7)$$

where \mathbf{X} are the global coordinates of the eight vertices defining the hex. Usually, Lagrange polynomials \mathbf{N} are shape functions for the regular element with $\xi, \eta, \zeta \in [0, 1]$. It follows that

$$\mathbf{X} = \begin{bmatrix} x_1 & \cdots & x_8 \\ y_1 & \cdots & y_8 \\ z_1 & \cdots & z_8 \end{bmatrix}, \mathbf{N}(\xi, \eta, \zeta) = \begin{bmatrix} (1-\xi)(1-\eta)(1-\zeta) \\ \xi(1-\eta)(1-\zeta) \\ \xi\eta(1-\zeta) \\ (1-\xi)\eta(1-\zeta) \\ (1-\xi)(1-\eta)\zeta \\ \xi(1-\eta)\zeta \\ \xi\eta\zeta \\ (1-\xi)\eta\zeta \end{bmatrix} \quad (8)$$

These functions ensure C^0 -continuity across adjacent elements and enable parametric representation of the distorted element geometry.

Using the differentiation from (7), the Jacobian matrix \mathbf{J} , which defines the local-to-global coordinate transformation, is

$$\mathbf{J} = \begin{bmatrix} \frac{\partial x}{\partial \xi} & \frac{\partial x}{\partial \eta} & \frac{\partial x}{\partial \zeta} \\ \frac{\partial y}{\partial \xi} & \frac{\partial y}{\partial \eta} & \frac{\partial y}{\partial \zeta} \\ \frac{\partial z}{\partial \xi} & \frac{\partial z}{\partial \eta} & \frac{\partial z}{\partial \zeta} \end{bmatrix} = \mathbf{X} \cdot \nabla \mathbf{N}, \quad (9)$$

where $\nabla \mathbf{N} = \begin{bmatrix} \frac{\partial \mathbf{N}}{\partial \xi} & \frac{\partial \mathbf{N}}{\partial \eta} & \frac{\partial \mathbf{N}}{\partial \zeta} \end{bmatrix}$.

While a bijective mapping requires a positive Jacobian determinant $|\mathbf{J}| > 0$ everywhere within an element, it remains an open problem to check the global minimum in the parameter space. An alternative approach, popularized by the visualization tool ParaView (3) and recent literature (6, 15, 17), is to evaluate the Jacobian at nine points: the eight corners and the element center in the parametric space. The minimum value from these nine points is then used as a metric for element quality. The objective of the following analysis is to provide guarantees for positivity at these nine points.

When the shape functions $\mathbf{N}(\xi, \eta, \zeta)$ are Lagrange polynomials, Equation 9 becomes a polynomial in m variables constrained to the hypercube $(0, 1)^m$. To prove that the Jacobian is positive within this domain, it is needed to rewrite it as a conic combination (i.e., a linear combination with non-negative coefficients) of basis polynomials that are all positive on this hypercube and ensure at least one coefficient is positive. Lagrange polynomials are not such a basis. This is evident from the one-dimensional case: the only Lagrange polynomials $\mathbf{N}(\xi)$ guaranteed to be positive over the entire interval $\xi \in (0, 1)$ are the four functions $1, \xi, 1 - \xi,$ and $\xi(1 - \xi)$. Any higher-order Lagrange polynomial will become negative on some part of the interval, regardless of node placement. This limitation necessitates the use of a positive polynomial basis, such as the Bernstein basis, which is inherently positive on $(0, 1)$ for any degree. For a parameter vector \mathbf{x} and its multiple indices $\mathbf{n} = (n_1, \dots, n_m)$, where n_j denotes the highest degree for the j -th variable, the Bernstein basis are $B_{\mathbf{i}, \mathbf{n}}(\mathbf{x}) = \prod_{j=1}^m \binom{n_j}{i_j} x_j^{i_j} (1 - x_j)^{n_j - i_j}$, where the parameter vector $\mathbf{x} = (x_1, \dots, x_m) \in (0, 1)^m$, and $\mathbf{i} = (i_1, \dots, i_m)$ satisfy $0 \leq i_j \leq n_j$ for all j . The transformation from monomial to Bernstein coefficients is given by Theorem 5.1.

Theorem 5.1. *Given integer $m \in \mathbb{N}_{\geq 1}$ and multiple indices $\mathbf{n} = (n_1, \dots, n_m) \in \mathbb{N}^m$, for a polynomial $\mathbf{J}(\mathbf{x}) = \sum_{\mathbf{0} \leq \mathbf{i} \leq \mathbf{n}} J_{\mathbf{i}} \prod_{j=1}^m x_j^{i_j}$ where the parameter vector $\mathbf{x} = (x_1, \dots, x_m) \in (0, 1)^m$, the multiple indices $\mathbf{i} = (i_1, \dots, i_m)$ satisfy $0 \leq i_j \leq n_j$ for all j . Then Bernstein expansion $\mathbf{J}(\mathbf{x}) = \sum_{\mathbf{0} \leq \mathbf{i} \leq \mathbf{n}} \beta_{\mathbf{i}} B_{\mathbf{i}, \mathbf{n}}(\mathbf{x})$, where $B_{\mathbf{i}, \mathbf{n}}(\mathbf{x}) = \prod_{j=1}^m \binom{n_j}{i_j} x_j^{i_j} (1 - x_j)^{n_j - i_j}$, has coefficients:*

$$\beta_{\mathbf{i}} = \sum_{\mathbf{0} \leq \mathbf{k} \leq \mathbf{i}} \prod_{j=1}^m \frac{\binom{i_j}{k_j}}{\binom{n_j}{k_j}} J_{\mathbf{k}}, \mathbf{0} \leq \mathbf{i} \leq \mathbf{n}. \quad (10)$$

Proof. Using the factorial definition of combinatorial

numbers, it holds that:

$$\binom{n_j - k_j}{i_j - k_j} = \frac{(n_j - k_j)!}{(i_j - k_j)!(n_j - i_j)!} = \frac{\binom{i_j}{k_j} \binom{n_j}{i_j}}{\binom{n_j}{k_j}}. \quad (11)$$

Using the binomial theorem and Equation 11, it holds that:

$$\begin{aligned} x_j^{k_j} &= x_j^{k_j} (x_j + (1 - x_j))^{n_j - k_j} \\ &= x_j^{k_j} \sum_{i_j=0}^{n_j - k_j} \binom{n_j - k_j}{i_j} x_j^{i_j} (1 - x_j)^{n_j - k_j - i_j} \\ &= \sum_{i_j=0}^{n_j - k_j} \binom{n_j - k_j}{i_j} x_j^{i_j + k_j} (1 - x_j)^{n_j - (i_j + k_j)} \\ &= \sum_{i_j=k_j}^{n_j} \binom{n_j - k_j}{i_j - k_j} x_j^{i_j} (1 - x_j)^{n_j - i_j} \\ &= \sum_{i_j=k_j}^{n_j} \frac{\binom{i_j}{k_j} \binom{n_j}{i_j}}{\binom{n_j}{k_j}} x_j^{i_j} (1 - x_j)^{n_j - i_j}. \end{aligned} \quad (12)$$

Therefore, beginning with the polynomial expansion of $\mathbf{J}(\mathbf{x})$, by substituting the expansion for each $x_j^{k_j}$ using Equation 12, interchanging the product and sum, and changing the summation order to factor out the basis functions $B_{\mathbf{i},\mathbf{n}}(\mathbf{x})$, it can be obtained

$$\begin{aligned} \mathbf{J}(\mathbf{x}) &= \sum_{\mathbf{0} \leq \mathbf{k} \leq \mathbf{n}} J_{\mathbf{k}} \prod_{j=1}^m x_j^{k_j} \\ &= \sum_{\mathbf{0} \leq \mathbf{k} \leq \mathbf{n}} J_{\mathbf{k}} \prod_{j=1}^m \left(\sum_{i_j=k_j}^{n_j} \frac{\binom{i_j}{k_j}}{\binom{n_j}{k_j}} \binom{n_j}{i_j} x_j^{i_j} (1 - x_j)^{n_j - i_j} \right) \\ &= \sum_{\mathbf{0} \leq \mathbf{k} \leq \mathbf{n}} J_{\mathbf{k}} \sum_{\mathbf{k} \leq \mathbf{i} \leq \mathbf{n}} \prod_{j=1}^m \frac{\binom{i_j}{k_j}}{\binom{n_j}{k_j}} \binom{n_j}{i_j} x_j^{i_j} (1 - x_j)^{n_j - i_j} \\ &= \sum_{\mathbf{0} \leq \mathbf{i} \leq \mathbf{n}} \left(\sum_{\mathbf{0} \leq \mathbf{k} \leq \mathbf{i}} \prod_{j=1}^m \frac{\binom{i_j}{k_j}}{\binom{n_j}{k_j}} J_{\mathbf{k}} \right) \prod_{j=1}^m \binom{n_j}{i_j} x_j^{i_j} (1 - x_j)^{n_j - i_j} \\ &= \sum_{\mathbf{0} \leq \mathbf{i} \leq \mathbf{n}} \beta_{\mathbf{i}} B_{\mathbf{i},\mathbf{n}}(\mathbf{x}). \end{aligned} \quad (13)$$

To this end, Equation 10 holds and the proof is done. \square

This proof extends the univariate case established in (29) Appendix B to the multivariate setting. Theorem 5.1 tells that the coefficients $\beta_{\mathbf{i}}$ of the Bernstein basis are related to the monomial coefficients $J_{\mathbf{i}}$ via the linear transformation.

Given an all-hex tessellation of the bounding box T_{AABB} and the SDF value at eight corners of each cell $h \in H_{\text{Int}(T_{\text{AABB}})}$ with respect to the input geometry

Table 1: Coordinates of twelve red points in Figure 5 in the local parametric space and in the global physical space.

Number	Local position	Global position
1	$(s_1, 0, 0)$	$s_1(x_2, y_2, z_2) + (1 - s_1)(x_1, y_1, z_1)$
2	$(0, s_2, 0)$	$s_2(x_4, y_4, z_4) + (1 - s_2)(x_1, y_1, z_1)$
3	$(0, 0, s_3)$	$s_3(x_5, y_5, z_5) + (1 - s_3)(x_1, y_1, z_1)$
4	$(1, s_4, 0)$	$s_4(x_3, y_3, z_3) + (1 - s_4)(x_2, y_2, z_2)$
5	$(1, 0, s_5)$	$s_5(x_6, y_6, z_6) + (1 - s_5)(x_2, y_2, z_2)$
6	$(s_6, 1, 0)$	$s_6(x_3, y_3, z_3) + (1 - s_6)(x_4, y_4, z_4)$
7	$(1, 1, s_7)$	$s_7(x_7, y_7, z_7) + (1 - s_7)(x_3, y_3, z_3)$
8	$(0, 1, s_8)$	$s_8(x_8, y_8, z_8) + (1 - s_8)(x_4, y_4, z_4)$
9	$(s_9, 0, 1)$	$s_9(x_6, y_6, z_6) + (1 - s_9)(x_5, y_5, z_5)$
10	$(0, s_{10}, 1)$	$s_{10}(x_8, y_8, z_8) + (1 - s_{10})(x_5, y_5, z_5)$
11	$(1, s_{11}, 1)$	$s_{11}(x_7, y_7, z_7) + (1 - s_{11})(x_6, y_6, z_6)$
12	$(s_{12}, 1, 1)$	$s_{12}(x_7, y_7, z_7) + (1 - s_{12})(x_8, y_8, z_8)$

T_{geom} , the MC algorithm reconstructs an isosurface. An edge is a sign-change edge if its two endpoints lie on opposite sides of the isosurface (one inside and one outside). For such edges, an intersection point is computed to represent the intersection of the reconstructed isosurface with the edge. As the cell graph structure is 3-regular, provided the intersection point lies within the edge's open interval (ensured numerically by clamping SDF values to non-zero values), the isosurface will intersect the cell into 3-regular polyhedra, with each being split into hexes via midpoint subdivision. In (9), thirty-three unique cases are identified based on the possible isosurface topologies within a cube. However, this classification contains a repetition between Case 12.2 and Case 12.3. Furthermore, if one considers mirror symmetry, Cases 11 and 14 are topologically identical. Therefore in total, thirty-one distinct cases remain for analysis.

Among the thirty-one cases, fourteen cases (Figure 6) can be proved that they generate positive Jacobian hexes under midpoint subdivision. Within the unit cube $[0, 1]^3$, the vertex coordinates of the hexes are enumerated, and the Jacobians are computed analytically. As in the left panel of Figure 5 and Table 1, the positions of the twelve red intersection points in the parametric space are defined by parameters $s_i \in (0, 1)$ for $i = 1, \dots, 12$. The use of an open interval avoids the generation of degenerate hexes. In practical code implementation, each s_i is clamped as $s_i = \max(\min(s_i, 1 - \epsilon), \epsilon)$, where ϵ is a small positive tolerance.

For the remaining seventeen cases (left picture of each case, Figure 7), the concave geometry of the resulting meshes makes such guarantees difficult to establish. While exploring less restrictive constraints on vertices is a potential direction for future work, it is found that aside from Cases 7-3 and 13-4, the other fifteen cases are exceptionally difficult to maintain positive Jacobians within one cell. Consequently, from an implementation standpoint, as shown in the middle picture of each case in Figure 7, a local refinement lookup table is established. For each case,

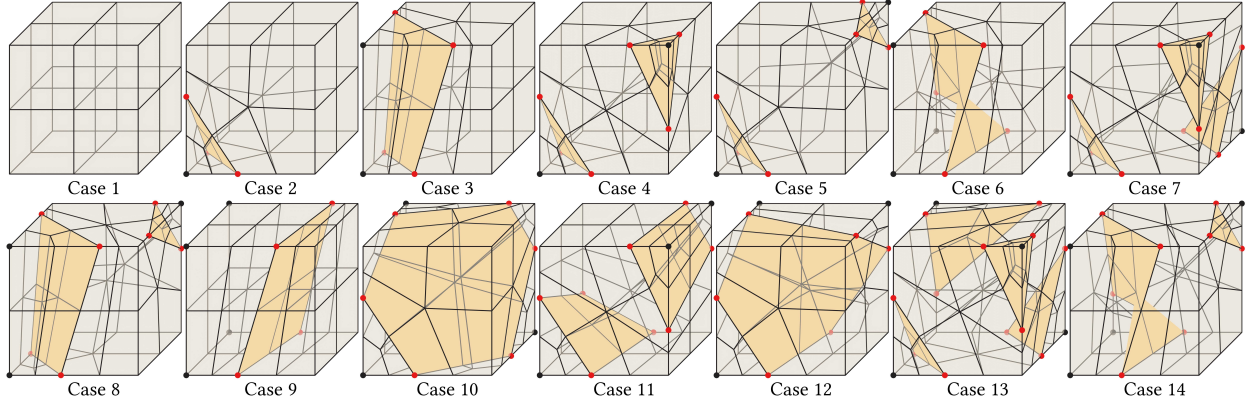


Figure 6: Fourteen topological cases that permit positive Jacobian proof. The unit cube cell is shaded in gray and the reconstructed isosurface is represented by yellow faces. Red points mark the intersections between the isosurface and cell edges. Grid points lying inside or outside input geometry $\text{Int}(T_{\text{geom}})$ are distinguished by the presence or absence of black dots. The cell is tessellated by the isosurface into 3-regular polyhedra and then subdivided via midpoint subdivision to yield all-hex meshes.

the left picture shows the triangulated isosurface to be reconstructed. The middle picture is the proposed local refinement method, where vertices inside the cell are assigned a virtual inside/outside status (represented by the presence or absence of a black dot). It can be verified that after local refinement, all cells fall into one of the fourteen topologies with positive Jacobian proofs. The right picture displays the reconstructed isosurface, with red dots indicating intersection points on sign-change edges. The reconstructed isosurface preserves the same topology as the triangulated version shown in the left picture. In this way, by refining the cell into multiple cells, the MCHex method achieves greater degree of freedom to represent these concave isosurfaces at the expense of a slight reduction in mesh quality. An important concern arises: in the physical space, to ensure that the locally refined cell shapes can be enumerated and guaranteed to produce positive Jacobians, the newly inserted interior vertices are placed at fixed positions. The true inside/outside status at these points can be different from the inside/outside status. To better understand this issue, in the bottom right picture of Figure 7, the true triangle surface of Case 4-1 is overlaid on the local refinement template. According to the true SDF values, the top-left and bottom-right points should not have black dots, which contradicts the template. This is referred to as *sign mismatching*. As a result, the reconstructed isosurface may be topologically correct but geometrically inaccurate. The accurate boundary recovery can only be deferred to subsequent heuristic optimization (without guarantee on the upper bounds of mesh quality or geometry accuracy). In the implementation, SDF values

for inserted vertices are first computed. When the computed sign contradicts the template requirement, the SDF values are adjusted to a minimal magnitude with the correct sign (e.g., modifying a computed value of 1 to -10^{-10} when the template requires the SDF value to be negative). This strategy maintains maximum fidelity to actual SDF values while only altering signs when strictly necessary. In summary, topological recovery is provided for all seventeen local refinement cases without any ambiguities (52, 53), but completely accurate boundary reconstruction for these cases remains a subject for future work.

This work considers the four transition cells introduced in (39). Figure 8 illustrates these four configurations handling face transitions as well as transitions across convex corners and edges. To reduce redundant validation effort, Theorem 5.2 is introduced to avoid repeatedly verifying the Jacobian for cells that are affine transformations of already validated ones.

Theorem 5.2. *Let A be a 3×3 invertible real matrix and $\omega(\mathbf{u}, \mathbf{v}, \mathbf{w})$ be the real directed volume of the parallelepiped formed by three vectors $\mathbf{u}, \mathbf{v}, \mathbf{w}$ in \mathbb{R}^3 . Then $\forall \mathbf{u}, \mathbf{v}, \mathbf{w} \in \mathbb{R}^3, \omega(A\mathbf{u}, A\mathbf{v}, A\mathbf{w}) = \det(A)\omega(\mathbf{u}, \mathbf{v}, \mathbf{w})$.*

Proof. Let $\mathbf{u}, \mathbf{v}, \mathbf{w}$ have components u^i, v^j, w^k in the standard basis. Then $\omega(\mathbf{u}, \mathbf{v}, \mathbf{w}) = \epsilon_{ijk} u^i v^j w^k$, where ϵ_{ijk} is the Levi-Civita symbol. The transformed vec-

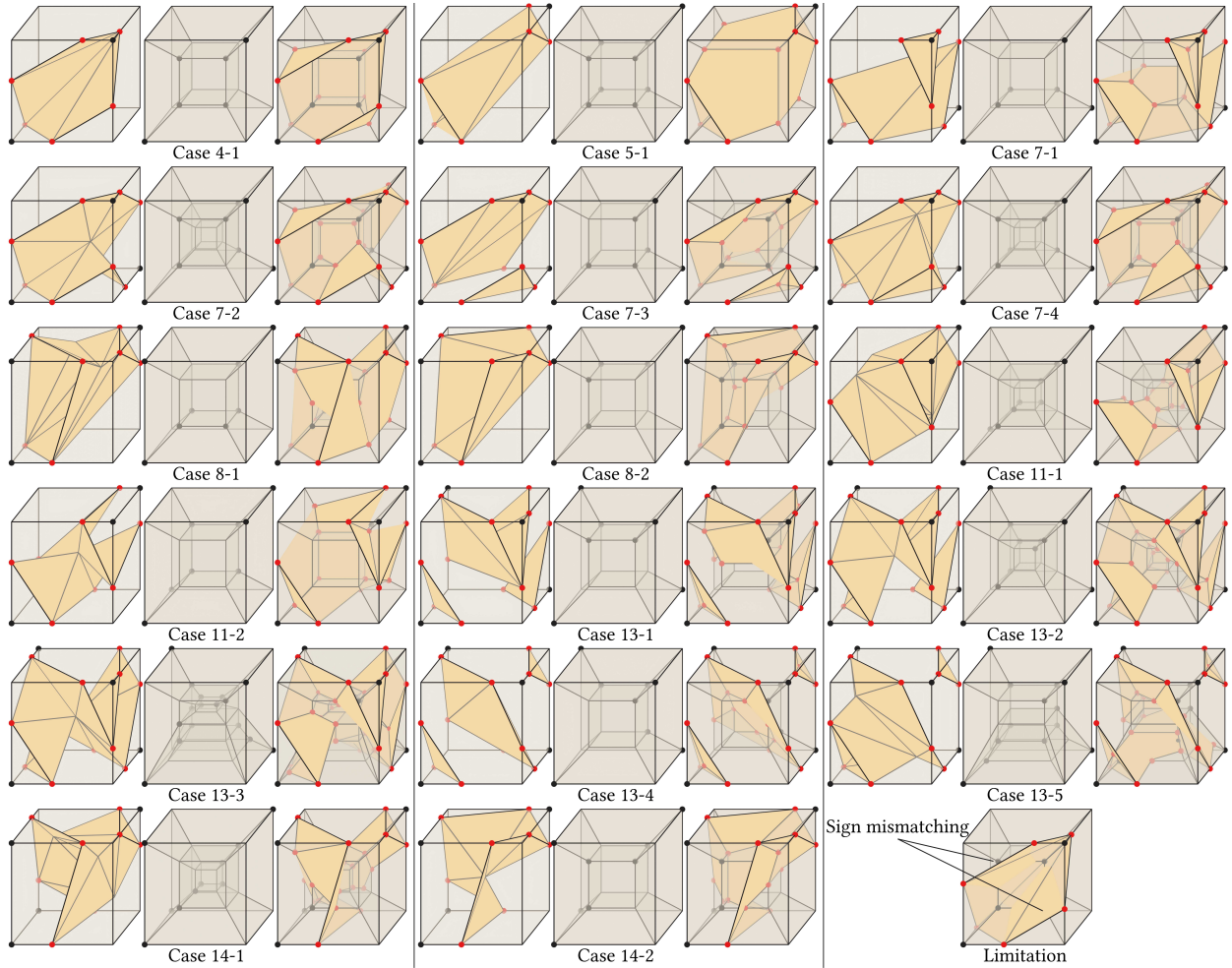


Figure 7: Seventeen topological cases for which a positive Jacobian cannot be guaranteed. For each case: the left picture shows the input triangle geometry; the middle picture shows the proposed local refinement template; the right picture shows the extracted isosurface after local refinement, where virtual SDF values assigned to new vertices ensure each hex falls into the fourteen proven topological cases and the isosurface topology is the same. Seven cases require two levels of local refinement. Using Case 4-1 as an example, the bottom right picture illustrates a limitation called *sign mismatching*: the true SDF values at eight internal insertion points may have opposing signs to the template’s requirements, causing a deviation between the reconstructed isosurface and the true surface.

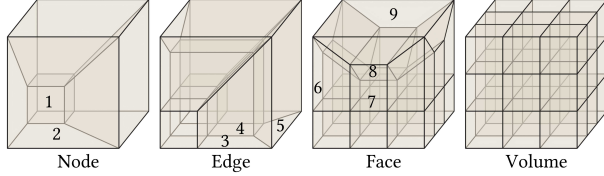


Figure 8: Four types of distinct transition cells proposed by (39). The enumerated cells represent the maximal set in which no two cells are affinely equivalent under orientation-preserving (positive-determinant) transformations.

tors can be written as

$$\begin{aligned}
 \omega(\mathbf{A}\mathbf{u}, \mathbf{A}\mathbf{v}, \mathbf{A}\mathbf{w}) &= \epsilon_{ijk}(\mathbf{A}\mathbf{u})^i(\mathbf{A}\mathbf{v})^j(\mathbf{A}\mathbf{w})^k \\
 &= \epsilon_{ijk}(A_i^j u^l)(A_m^j v^m)(A_n^k w^n) \\
 &= (\epsilon_{ijk} A_i^j A_m^j A_n^k) u^l v^m w^n \\
 &= \det(A) \epsilon_{lmn} u^l v^m w^n \\
 &= \det(A) \omega(\mathbf{u}, \mathbf{v}, \mathbf{w}).
 \end{aligned}$$

□

The theorem tells that if cell $h_1(V_1, E_1, Q_1)$ can affinely transfer to cell $h_2(V_2, E_2, Q_2)$ via $T(\mathbf{x}) = \mathbf{A}\mathbf{x} + \mathbf{b}$ with $\det(A) > 0$, then for any three vectors $\mathbf{u}, \mathbf{v}, \mathbf{w}$ in h_1 that form a positively oriented volume $\omega(\mathbf{u}, \mathbf{v}, \mathbf{w}) > 0$, their images $\mathbf{A}\mathbf{u}, \mathbf{A}\mathbf{v}, \mathbf{A}\mathbf{w}$ in h_2 will also form a positively oriented volume $\omega(\mathbf{A}\mathbf{u}, \mathbf{A}\mathbf{v}, \mathbf{A}\mathbf{w}) > 0$.

The enumerated 9 cells in Figure 8 forms a maximal set in which no two cells are affinely equivalent under orientation preserving transformations (i.e., those with a positive determinant matrix A). The first level of local refinement in Figure 7 subdivides each of these base cells by connecting its eight grid points to its centroid, resulting in seven smaller children cells. This process introduces 15 new, affinely unique cell types to the maximal set. In specific configurations, such as Case 13-5 in Figure 7, a second refinement level is applied, contributing one additional unique cell type. The maximal set thus comprises 25 unique cell types in total. Each of these cells is mapped from a unit parametric cell via trilinear interpolation under 24 distinct rotational configurations. These rotations form the cube’s rotational symmetry group, known as the octahedral group, which has an order of 24. This order is derived from the 8 possible vertices a given vertex can be mapped to, multiplied by the 3 rotational symmetries ($0^\circ, 120^\circ, 240^\circ$) that keep that vertex fixed (i.e., $8 \times 3 = 24$). Using this framework, all Bernstein coefficients are computed for the nine-point Jacobian determinant of every hex element generated via midpoint subdivision in Figure 6, covering all 25 cell types and all 24 rotational configurations.

In the beginning, the code attempts to validate that all hexes have positive Jacobian using the naïve midpoint subdivision. A hex is considered to have a positive Jacobian if the minimum Bernstein coefficient is non-negative and the maximum Bernstein coefficient is positive (to prevent all-zero results). The results reveal that only Case 12 and Case 14 fail to ensure the condition. For Case 12, a small displacement of the volume center suffices to restore all positive Jacobians. For Case 14, even after adjusting the volume center, a small number of configurations still yield non-positive Jacobians. This issue is resolved further by implementing a piecewise strategy based on the positions of points 7, 11, and 12 along their respective edges, as illustrated in Figure 5. The edge parameter space is partitioned into intervals and apply distinct volume center offsets within each interval. This piecewise strategy successfully guarantees positive Jacobians for Case 14. The complete Python code used to perform the whole proof, along with a detailed explanation, is provided in Appendix A and the Supplementary Materials.

6 Results and Applications

To validate the MCHex approach, a C++ prototype is implemented following Algorithm 1 and evaluated on the Thingi10K dataset (55) through batch processing. The boundary recovery performance is quantified using the IoU and the HR, which measure the volumetric alignment between the input geometry $\text{Int}(T_{\text{geom}})$ and the hex mesh boundary $\text{Int}(\partial H_{\text{Int}(T_{\text{geom}})})$, as well as the surface alignment between T_{geom} and $\partial H_{\text{Int}(T_{\text{geom}})}$. A comparative analysis between the MCHex and the RO method is conducted to demonstrate the superior boundary convergence rate of MCHex. For each model, an SDF is precomputed on 3-refinement grids. This SDF is then used by both methods to extract the interior hex mesh $H_{\text{Int}(T_{\text{geom}})}$, where in the RO baseline, a cell is included if the sum of the SDF values at its eight vertices is positive.

To enable the batch processing of all 10,000 meshes from the Thingi10K dataset in a reasonable time and without cherry-picking, the grid initialization is configured to split all cells that have error-sensitive function exceeding 0.05. The computation times for both RO and MCHex methods are shown in the left panel of Figure 9. Analysis of the time data and code implementation reveals that the overall execution time scales linearly with the product of triangle face count and hex mesh vertex count. This linear relationship is primarily attributed to the SDF computation. While

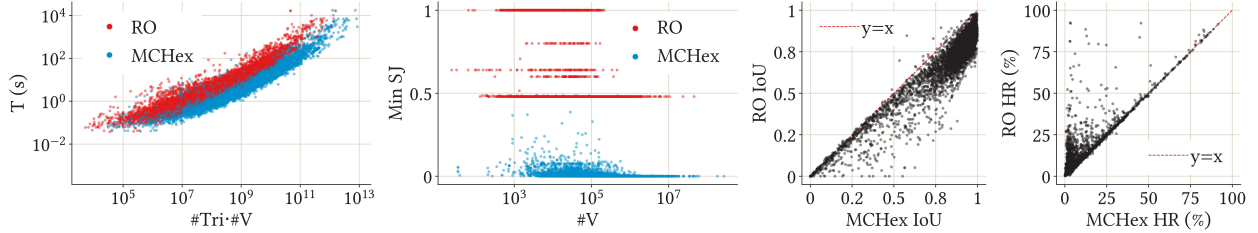


Figure 9: Comparison of the RO and MCHex methods. From left to right: Computation time complexity versus the product of triangle face count and hex-mesh vertex count; Minimum scaled Jacobian of the resulting meshes versus the number of vertices; One-to-one comparison of IoU values between MCHex and RO; One-to-one comparison of HR values between MCHex and RO.

other operations, including file I/O, grid refinement, and isosurface extraction, also scale linearly with hex mesh vertex count, their constant overhead is more significant for models with a low $\#Tri \cdot \#V$ product value. This explains the flat curve in the data in the beginning. As the product increases, SDF computation dominates the pipeline’s execution time, causing the data points to converge toward a linear trend. Moreover, given the current SDF implementation is not optimized, there should be significant potential for accelerating the entire pipeline in the future implementation.

The minimum scaled Jacobian of the meshes generated by the RO and MCHex methods is plotted against the number of vertices in the resulting hex meshes in the second panel from the left in Figure 9. The scaled Jacobian for the RO method clusters at discrete values between 0.48 and 1.0. These specific values correspond directly to the predetermined Jacobian values of the hex elements in the 3-refinement templates. The scaled Jacobian for the MCHex method is verified to be greater than zero for all generated meshes, which is consistent with the prior theoretical analysis. Moreover, for a given background grid, the minimum scaled Jacobian achieved by the MCHex method will never exceed that of the RO method. This is because the cutting operations in the MCHex method, while preserving positivity, do not improve the quality metric of the original cell and can only maintain or degrade it.

A direct, one-to-one comparison of IoU and HR between RO and MCHex meshes generated from the same SDF are presented in the right two panels in Figure 9 respectively. This can be considered a fixed-computation-budget comparison, as both meshes share the primary computational bottleneck of SDF generation. In this view, most points lie below the $y = x$ line, indicating that for a fixed computational budget, the MCHex method consistently produces hex meshes that more accurately conform to the input geometry.

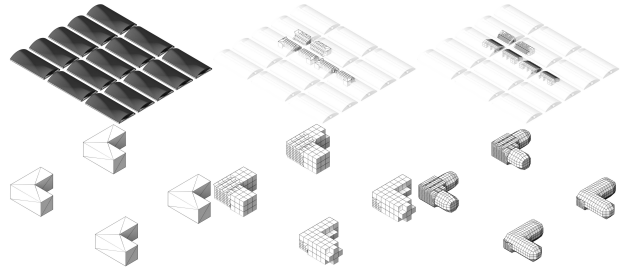


Figure 10: The only two modes where MCHex produces lower IoU or higher HR than RO method. From left to right: the input geometry, meshes from the RO method, and meshes from the MCHex method. Top ($\#1514499$): Both methods fail to capture thin shell geometry due to insufficient resolution threshold (0.05), meshing only a portion in the middle. Bottom ($\#92834$): Axis-aligned surfaces. For both modes, RO’s axis-aligned facets provide an inherent advantage to occupy more volumes in the triangle mesh.

A few cases where the MCHex method yielded a slightly lower IoU/higher HR than RO are manually inspected, and all instances can be categorized into two types in Figure 10. The first type, exemplified by model $\#1514499$ (top row), occurs when the fixed error threshold (0.05) is too coarse to capture thin shells. This leads to extensive hollow regions in both meshes, constituting failed meshing for both methods. In these cases, the MCHex method, which tends to produce rather a smoothed surface than an axis-aligned surface, results in a slightly lower IoU (e.g., 0.0391 for MCHex vs. 0.0420 for RO) and a slightly higher HR (e.g., 33.7% for MCHex vs. 34.1% for RO). The difference, however, is negligible and both outcomes are unsatisfactory. The second type, shown for model $\#92834$ (bottom row), involves input geometries that are inherently axis-aligned. Here, the RO method, which preserves axis-aligned facets, holds a natural advantage. The MCHex method’s boundary smoothing slightly reduces its IoU (0.816) compared to RO (0.823), and slightly increases its HR (2.79%)

compared to RO (2.28%) in this specific scenario. Beyond these two explicable patterns, no other instances have been observed where the MCHex method is outperformed by the RO method under the same background grid.

MCHex successfully generates all-hex meshes with strictly positive Jacobians on 100% of the geometries tested. To benchmark its robustness against state-of-the-art hex meshing tools, a comparison is made with two significant studies in the past: one utilizing the commercial software MeshGems (37), and another is (15). In the MeshGems study, 4,050 hex meshes are produced out of 10,000 attempts; among them, 25 meshes contain invalid elements with negative Jacobians. Due to the slow computational speed of (15), which could take anywhere from several minutes to days per model, a full-dataset comparison is infeasible. For the 25 models that produced negative Jacobians with MeshGems, hex meshes of comparable scale using (15) and MCHex are generated, with particular attention to ensuring that the vertex count of MCHex is slightly lower than that of the corresponding MeshGems mesh. The resulting MCHex meshes are further smoothed using (43). Due to the slow convergence of the optimization algorithm in complex meshes, the process is terminated for some meshes before full convergence is reached. A comprehensive comparison is then conducted, evaluating the number of vertices, minimum scaled Jacobian, IoU, and HR metrics.

As illustrated in Figure 11, six representative examples are selected from the 25 models for visualization. In the triangular surface meshes of row 1 (#135757) and row 2 (#338508), outward-facing triangles are colored white, while inward-facing ones are marked red. It is hypothesized that the inconsistent normal directions caused issues for the first two methods, which rely on dihedral angle-based subdivision strategies, resulting in their failure to produce valid hex meshes. In contrast, MCHex uses SDF interpolation error to guide subdivision, making it robust to normal noise and thus capable of generating valid hex meshes. When the vertex budget is low, MCHex exhibits weaker surface approximation capability than (15) due to the 3-refinement scheme. However, as the vertex count increases, MCHex surpasses the latter, since (15) encounters fitting problems along red-white triangle boundaries. MeshGems performed poorly, largely because it failed to mesh the left part.

In the triangular surface meshes of row 3 (#1508789) and row 4 (#1004827), self-intersecting triangles are colored red. These self-intersections lead to ambiguities in inside/outside classification, which likely caused MeshGems to fail in capturing

most of the geometry in row 4. (15) operates by identifying and meshing each connected component independently, partitioned the model in row 3 into over 1,000 separate components. This resulted in a hex mesh with an excessively high vertex count and self-intersections. In contrast, MeshGems and MCHex process the input as a single connected volume, thereby avoiding such self-intersections in the resulting hex mesh. However, for MCHex, certain regions where one component deeply penetrates another may be interpreted as interior by the SDF. As a consequence, the distance from these points to the hex mesh surface cannot be effectively reduced through increasing vertex budget. This explains why the IoU metric improves with increasing vertex count in the plots, while the HR remains unchanged. In row 4, (15) produces distorted results, likely due to erroneous inside/outside judgments. By leveraging the robustness of the SDF representation, MCHex is able to generate better hex meshes.

In the triangular surface meshes of row 5 (#138102) and row 6 (#138180), all edges are non-manifold, and consequently, every triangle adjacent to these edges is colored red. The non-manifoldness arises from multiple definitions of the same triangular face, leading to inconsistent inside/outside determinations in MeshGems and resulting in poor boundary fitting. In contrast, both (15) and MCHex correctly distinguish interior from exterior.

There are two main limitations of MCHex. First, as most models in the Thingi10K dataset contain sharp edges and corners, MCHex is unable to preserve these features due to the inherent smoothing nature of the MC approach. As a result, sharp details such as gear teeth, fan blades, and engraved letter edges are lost. Second, the use of a 3-refinement template, which only allows convex grid depth transitions, unnecessarily refines too many areas. For hollow-shell models with intricate surface details, the entire interior volume is refined to the same level as the surface, significantly increasing vertex count and computational cost. Furthermore, 3-refinement is inherently less efficient than 2-refinement. Nevertheless, MCHex achieves superior boundary fitting with fewer vertices than the other two methods in most models. Furthermore, as vertex count increases, MCHex consistently improves IoU while reducing HR, whereas the competing methods, relying solely on projection and smoothing for surface fitting, suffer from negative Jacobians or degrading boundary fitting due to the constraints required to maintain positive Jacobians as optimization complexity grows. There are mainly three reasons. First, MCHex saves vertex count through its natural boundary pillowing,

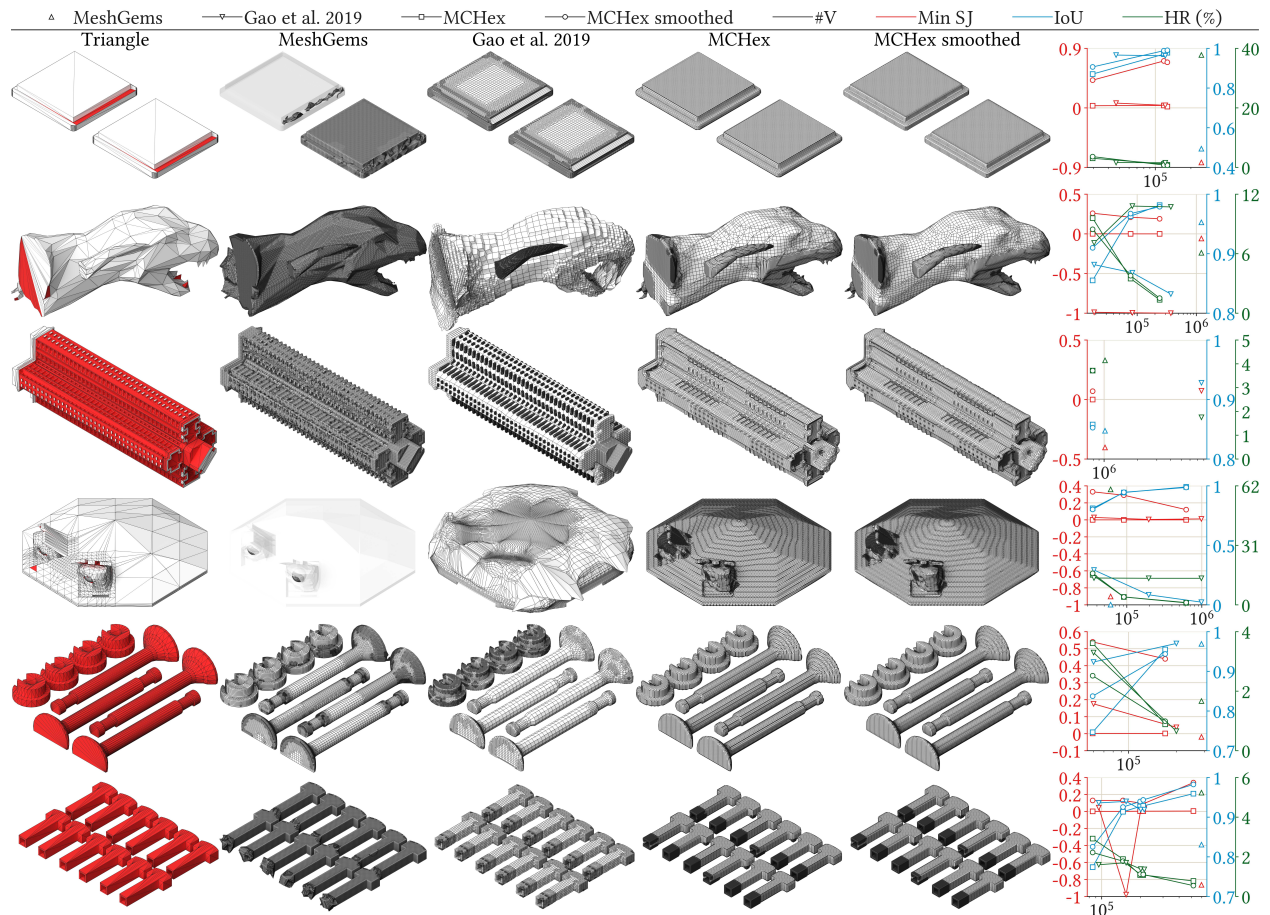


Figure 11: MeshGems fails to maintain all positive Jacobians on some simple geometries in Thing10K (55). Six of them are selected and hex-meshing methods are compared using them. In the first two rows, models contain inconsistent surface normals, and inward-facing triangles are highlighted in red. The third and fourth rows contain self-intersecting triangles, also marked in red. The fifth and sixth rows consist entirely of non-manifold edges; thus, all triangles adjacent to such edges are colored red. For each model, hex meshes are generated with comparable vertex counts using MeshGems, (15), MCHex, and MCHex with smoothing (43), while ensuring that MCHex uses slightly fewer vertices than the former two. Each method is evaluated using the minimum scaled Jacobian, IoU, and HR. Despite being constrained by 3-refinement templates to guarantee all-positive Jacobians and lack of sharp edge preservation due to the intrinsic nature of the MC approach, MCHex achieves better boundary fitting in most cases, with fewer vertices.

which is particularly advantageous for models with large surface areas. This built-in pillowing eliminates the need for introducing an additional layer of elements. Second, it follows an Occam’s razor principle, producing meshes with clean and predictable boundary topology. Third, it uses SDF interpolation error, rather than explicit metrics such as dihedral angles or ray-intersection lengths computed on the explicit triangle mesh, to guide grid refinement. This allows MCHex to reliably compute an implicit SDF and extract a hex mesh with all-positive Jacobians from any input triangle mesh, even from ill triangle-soup geometries in real-world datasets.

The true strength of MCHex lies in its significant expansion of the geometric domain amenable to hex meshing. Within the Thing10K dataset, numerous models exist for which neither MeshGems nor (15) can generate satisfactory meshes. As shown in Figure 12, these two methods fail to produce hex meshes on exhibited models, within a 10-hour time limit, while the MCHex method succeeds and simultaneously achieves an IoU greater than 0.9 (a reasonable threshold for boundary fitting accuracy) and guarantees all-positive Jacobians.

The hex meshes generated by the MCHex method can be further improved through post-processing techniques such as geometric smoothing (43) or singularity structure simplification (14). For demonstration, another three relatively simple examples that MeshGems fails to maintain positive Jacobians are selected and presented in Figure 13. The corresponding mesh statistics are summarized in Table 2. Here, a regular point is defined as an interior point adjacent to eight hexes or a boundary point adjacent to four hexes. Similarly, a regular edge refers to an interior edge incident to four hexes or a boundary edge incident to two hexes. After smoothing, the minimum scaled Jacobian shows significant improvement, and the edge ratio is effectively reduced. The IoU also increases. The proportion of regular points and edges remains unchanged, as smoothing only warps the vertex positions without altering the mesh topology. In contrast, after singularity simplification, the minimum scaled Jacobian decreases slightly but remains acceptable. The edge ratio is further reduced in the first two models due to the removal of transition cells. In the third model, however, the edge ratio remains similar since the original mesh is already nearly uniform. Meanwhile, the proportion of regular points and edges increases in all cases, indicating a more structured singularity structure. It is worth noting that the simplification process is computationally expensive, typically taking over ten hours to complete. Moreover, when applied to more com-

plex models, the robustness of the simplification procedure becomes an issue. For instance, in the third model, the simplified mesh exhibits zigzag artifacts along originally smooth boundary curves, a problem that becomes more serious in more complex cases and often leads to simplification failures.

7 Conclusion and Future Work

This paper introduces a new paradigm MCHex for boundary handling in grid-based hex meshing by replacing the conventional pipeline of element removal and heuristic projection with a robust methodology based on MC-based cutting and midpoint subdivision. Founded on 3-regular graphs and midpoint subdivision, MCHex guarantees all-positive Jacobian values for every hex element while intrinsically providing boundary pillowing, resolving topological ambiguities, and yielding manifold surfaces for arbitrarily complex geometries. The algorithm exhibits time complexity linear in the product of the input triangle mesh size and grid size. Extensive validation demonstrates that the proposed framework converges to the boundary faster than RO method and successfully meshes challenging geometries where current leading commercial and academic solutions fail, offering an automatic and reliable pipeline for numerical simulation that integrates seamlessly with existing mesh quality post-processing algorithms.

Some limitations and future directions are also identified. First, the midpoint subdivision strategy inherently increases hex element count, imposing greater computational burden in subsequent numerical simulations. This limitation could be mitigated by adopting the vertex-efficient refinement approach in Figure 14, which prevents the midpoint subdivision from propagating to all internal cells. Second, the current theoretical guarantee of positive Jacobian is restricted to basic 3-refinement templates, which can lead to excessive refinement. Extending this proof to improved 3-refinement or 2-refinement templates would substantially reduce element counts while maintaining quality guarantees. Third, the method cannot preserve sharp features while ensuring positive Jacobian, a limitation inherent to the standard MC algorithm. A recent work demonstrates that incorporating additional feature-aware vertices on the isosurface and combining with deep learning can effectively preserve sharp edges (8). Adapting the proposed tessellation templates to redesign templates in Figure 6 and Figure 7 would possibly enable sharp feature preservation within this framework.



Figure 12: Under a 10-hour time budget, MCHex generates hex meshes on complex models from the Thingi10K dataset with both positive Jacobian and $\text{IoU} > 0.9$, while MeshGems and (15) fail. Twenty-two meshes are shown, with input geometries: #866925, #76475, #135807, #44375, #114029, #1041448, #1074637, #940414, #551075, #321050, #136074, #252784, #669972, #147736, #55280, #888464, #117641, #87688, #97866, #498974, #971425, and #372114.

Table 2: Statistics of the raw, smoothed (using (43)), and simplified (using (14)) MCHex models in Figure 13. Each cell contains three values separated by “/”, corresponding to the raw, smoothed, and simplified meshes, respectively.

Index	Minimum scaled Jacobian	Edge ratio	IoU	#Regular point/#All point	#Regular edge/#All edge
#83022	0.0000572/0.360/0.228	5,996,900/1,234/31	0.990/0.994/0.991	0.913/0.913/0.960	0.966/0.966/0.985
#96564	0.000370/0.390/0.303	14,686,700/4,579/35	0.932/0.978/0.966	0.800/0.800/0.938	0.921/0.921/0.976
#138183	0.00395/0.420/0.191	689/37/43	0.970/0.989/0.981	0.934/0.934/0.958	0.976/0.976/0.984

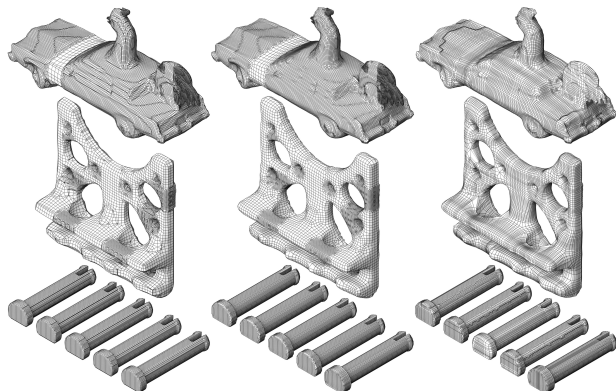


Figure 13: The MCHex mesh can be smoothed or simplified. From left to right: raw, smoothed and structurally simplified meshes. The last model contains some sharp features. While simplification effectively reduces irregularities, it occasionally produces poorly-shaped boundary elements with high edge ratios, presenting a limitation for scaling to larger meshes.

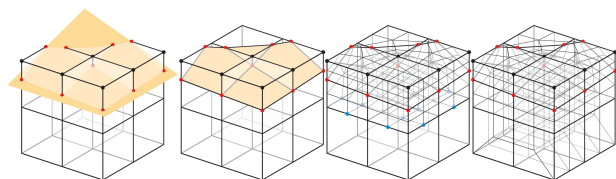


Figure 14: A proposed future direction for reducing vertex budget in MCHex. Left 1: Input triangle surface (yellow) intersecting the grid, with four upper cells penetrated by the surface and four lower cells located entirely inside the geometry; external grid points are shown as black dots, while intersection points are red dots. Left 2: Isosurface (yellow) reconstructed via Marching Cubes. Right 2: Only cells intersected by the triangle mesh undergo midpoint subdivision, creating hanging nodes (blue) on interfaces between intersected cells and internal cells. Right 1: Hanging nodes are eliminated using 2-refinement templates instead of applying the 1-to-8 subdivision from Case 1 of Figure 6 to all internal cells, significantly reducing the internal vertex count.

References

- [1] C. G. ARMSTRONG, H. J. FOGG, C. M. TIERNEY, AND T. T. ROBINSON, *Common themes in multi-block structured quad/hex mesh generation*, Procedia Engineering, 124 (2015), pp. 70–82.
- [2] M. A. AWAD, A. A. RUSHDI, M. A. ABBAS, S. A. MITCHELL, A. H. MAHMOUD, C. L. BAJAJ, AND M. S. EBEIDA, *All-hex meshing of multiple-region domains without cleanup*, Procedia Engineering, 163 (2016), pp. 251–261.
- [3] U. AYACHIT, *The ParaView Guide: A Parallel Visualization Application*, Kitware, Inc., Clifton Park, NY, USA, 2015.
- [4] S. BENZLEY, E. PERRY, K. MERKLEY, B. CLARK, AND G. SJAARDEMA, *A comparison of all hexagonal and all tetrahedral finite element meshes for elastic and elasto-plastic analysis*, Proceedings, 4th International Meshing Roundtable, 17 (1995).
- [5] T. BLACKER, *Meeting the challenge for automated conformal hexahedral meshing*, in 9th International Meshing Roundtable, Albuquerque, NM, USA, 2000, Citeseer, Sandia National Laboratories, pp. 11–20.
- [6] M. BRACCI, M. TARINI, N. PIETRONI, M. LIVESU, AND P. CIGNONI, *Hexalab.net: An online viewer for hexahedral meshes*, Computer-Aided Design, 110 (2019), pp. 24–36.
- [7] S. CANANN, *Plastering-a new approach to automated, 3-d hexahedral mesh generation*, in 33rd Structures, Structural Dynamics and Materials Conference, Dallas, Texas, USA, 1992, AIAA, p. 2416.
- [8] Z. CHEN AND H. ZHANG, *Neural marching cubes*, ACM Transactions on Graphics (TOG), 40 (2021), pp. 1–15.
- [9] E. V. CHERNYAEV, *Marching Cubes 33: Construction of Topologically Correct Isosurfaces*, tech. rep., CERN, Geneva, 1995.

- [10] A. O. CIFUENTES AND A. KALBAG, *A performance study of tetrahedral and hexahedral elements in 3-d finite element structural analysis*, Finite Elements in Analysis and Design, 12 (1992), pp. 313–318.
- [11] COREFORM, *Coreform cubit*. <https://coreform.com/products/coreform-cubit/government/>, 2025. Accessed: 2025-09-25.
- [12] M. S. EBEIDA, A. PATNEY, J. D. OWENS, AND E. MESTREAU, *Isotropic conforming refinement of quadrilateral and hexahedral meshes using two-refinement templates*, International Journal for Numerical Methods in Engineering, 88 (2011), pp. 974–985.
- [13] A. H. ELSHEIKH AND M. ELSHEIKH, *A consistent octree hanging node elimination algorithm for hexahedral mesh generation*, Advances in Engineering Software, 75 (2014), pp. 86–100.
- [14] X. GAO, D. PANOZZO, W. WANG, Z. DENG, AND G. CHEN, *Robust structure simplification for hex re-meshing*, ACM Transactions on Graphics (TOG), 36 (2017), pp. 1–13.
- [15] X. GAO, H. SHEN, AND D. PANOZZO, *Feature preserving octree-based hexahedral meshing*, Computer Graphics Forum, 38 (2019), pp. 135–149.
- [16] J. GREGSON, A. SHEFFER, AND E. ZHANG, *All-hex mesh generation via volumetric polycube deformation*, Computer Graphics Forum, 30 (2011), pp. 1407–1416.
- [17] H.-X. GUO, X. LIU, D.-M. YAN, AND Y. LIU, *Cut-enhanced polycube-maps for feature-aware all-hex meshing*, ACM Transactions on Graphics (TOG), 39 (2020), pp. 106–1.
- [18] A. HATCHER, *Algebraic Topology*, Cambridge University Press, Cambridge, UK, 2001.
- [19] K. HU, J. QIAN, AND Y. ZHANG, *Adaptive all-hexahedral mesh generation based on a hybrid octree and bubble packing*, in Proceedings of the 22nd International Meshing Roundtable, Berlin, Heidelberg, 2013, Springer.
- [20] INTRINSIM, *Meshgems: The standard for meshing technology*. <https://intrinsic.com/MeshGems.html>, 2025. Accessed: 2025-09-25.
- [21] Y. ITO, A. M. SHIH, AND B. K. SONI, *Octree-based reasonable-quality hexahedral mesh generation using a new set of refinement templates*, International Journal for Numerical Methods in Engineering, 77 (2009), pp. 1809–1833.
- [22] X. LIANG, M. S. EBEIDA, AND Y. ZHANG, *Guaranteed-quality all-quadrilateral mesh generation with feature preservation*, Computer Methods in Applied Mechanics and Engineering, 199 (2010), pp. 2072–2083.
- [23] X. LIANG AND Y. ZHANG, *Hexagon-based all-quadrilateral mesh generation with guaranteed angle bounds*, Computer Methods in Applied Mechanics and Engineering, 200 (2011), pp. 2005–2020.
- [24] ———, *An octree-based dual contouring method for triangular and tetrahedral mesh generation with guaranteed angle range*, Engineering with Computers, 30 (2014), pp. 211–222.
- [25] H. LIN, S. JIN, H. LIAO, AND Q. JIAN, *Quality guaranteed all-hex mesh generation by a constrained volume iterative fitting algorithm*, Computer-Aided Design, 67 (2015), pp. 107–117.
- [26] H. LIU, P. ZHANG, E. CHIEN, J. SOLOMON, AND D. BOMMES, *Singularity-constrained octahedral fields for hexahedral meshing*, ACM Transactions on Graphics (TOG), 37 (2018), p. 93.
- [27] M. LIVESU, L. PITZALIS, AND G. CHERCHI, *Optimal dual schemes for adaptive grid based hexmeshing*, ACM Transactions on Graphics (TOG), 41 (2021), pp. 1–14.
- [28] L. MARÉCHAL, *Advances in octree-based all-hexahedral mesh generation: Handling sharp features*, in Proceedings of the 18th International Meshing Roundtable, Springer, Berlin, Heidelberg, 2009, pp. 65–84.
- [29] R. J. MATHAR, *Orthogonal basis function over the unit circle with the minimax property*, 2018.
- [30] S. A. MITCHELL AND T. J. TAUTGES, *Pillowing doublets: Refining a mesh to ensure that faces share at most one edge*, tech. rep., Sandia National Lab.(SNL-NM), Albuquerque, NM (United States), 1995.
- [31] M. NIESER, U. REITEBUCH, AND K. POLTHIER, *Cubecover—parameterization of 3d volumes*, Computer Graphics Forum, 30 (2011), pp. 1397–1406.
- [32] S. J. OWEN, *A survey of unstructured mesh generation technology*, 7th International Meshing Roundtable, 3 (2000).

- [33] S. J. OWEN, R. M. SHIH, AND C. D. ERNST, *A template-based approach for parallel hexahedral two-refinement*, Computer-Aided Design, 85 (2017), pp. 34–52.
- [34] N. PIETRONI, M. CAMPEN, A. SHEFFER, G. CHERCHI, D. BOMMES, X. GAO, R. SCATENI, F. LEDOUX, J. REMACLE, AND M. LIVESU, *Hex-mesh generation and processing: A survey*, ACM Transactions on Graphics (TOG), 42 (2022), pp. 1–44.
- [35] L. PITZALIS, M. LIVESU, G. CHERCHI, E. GOBBETTI, AND R. SCATENI, *Generalized adaptive refinement for grid-based hexahedral meshing*, ACM Transactions on Graphics (TOG), 40 (2021), pp. 1–13.
- [36] A. A. RUSHDI, S. A. MITCHELL, A. H. MAHMOUD, C. C. BAJAJ, AND M. S. EBEIDA, *Allquad meshing without cleanup*, Computer-Aided Design, 85 (2017), pp. 83–98.
- [37] T. SCHNEIDER, Y. HU, X. GAO, J. DUMAS, D. ZORIN, AND D. PANOZZO, *A large-scale comparison of tetrahedral and hexahedral elements for solving elliptic pdes with the finite element method*, ACM Transactions on Graphics (TOG), 41 (2022), pp. 1–14.
- [38] R. SCHNEIDERS, *Algorithms for quadrilateral and hexahedral mesh generation*, Proceedings of the VKI Lecture Series on Computational Fluid Dynamic, VKI-LS, 4 (2000).
- [39] ———, *Octree-based hexahedral mesh generation*, International Journal of Computational Geometry & Applications, 10 (2000), pp. 383–398.
- [40] J. F. SHEPHERD AND C. R. JOHNSON, *Hexahedral mesh generation constraints*, Engineering with Computers, 24 (2008), pp. 195–213.
- [41] T. J. TAUTGES, *The generation of hexahedral meshes for assembly geometry: Survey and progress*, International Journal for Numerical Methods in Engineering, 50 (2001), pp. 2617–2642.
- [42] H. TONG, E. HALILAJ, AND Y. J. ZHANG, *Hybridoctree_hex: Hybrid octree-based adaptive all-hexahedral mesh generation with jacobian control*, Journal of Computational Science, 78 (2024), p. 102278.
- [43] H. TONG AND Y. J. ZHANG, *Fast and robust hexahedral mesh optimization via augmented lagrangian, l-bfgs, and line search*, in Proceedings of the 2025 SIAM International Meshing Roundtable, SIAM, Philadelphia, PA, 2025, pp. 24–33.
- [44] E. WANG, T. NELSON, AND R. RAUCH, *Back to elements-tetrahedra vs. hexahedra*, in Proceedings of the 2004 International ANSYS Conference, Pittsburgh, PA, USA, 2004, ANSYS Inc.
- [45] W. WANG, Y. CAO, AND T. OKAZE, *Comparison of hexahedral, tetrahedral and polyhedral cells for reproducing the wind field around an isolated building by les*, Building and Environment, 195 (2021), p. 107717.
- [46] Y. YU, X. WEI, A. LI, J. G. LIU, J. HE, AND Y. J. ZHANG, *Hexgen and hex2spline: Polycube-based hexahedral mesh generation and spline modeling for isogeometric analysis applications in ls-dyna*, in Geometric Challenges in Isogeometric Analysis, C. Manni and H. Speleers, eds., Cham, 2022, Springer International Publishing, pp. 333–363.
- [47] Y. ZHANG, *Challenges and advances in image-based geometric modeling and mesh generation*, in Image-Based Geometric Modeling and Mesh Generation, Springer, Dordrecht, The Netherlands, 2013, pp. 1–10.
- [48] Y. ZHANG AND C. BAJAJ, *Adaptive and quality quadrilateral/hexahedral meshing from volumetric data*, Computer Methods in Applied Mechanics and Engineering, 195 (2006), pp. 942–960.
- [49] Y. ZHANG, C. BAJAJ, AND B.-S. SOHN, *3d finite element meshing from imaging data*, Computer Methods in Applied Mechanics and Engineering, 194 (2005), pp. 5083–5106.
- [50] Y. ZHANG, T. J. HUGHES, AND C. L. BAJAJ, *An automatic 3d mesh generation method for domains with multiple materials*, Computer Methods in Applied Mechanics and Engineering, 199 (2010), pp. 405–415.
- [51] Y. ZHANG, X. LIANG, AND G. XU, *A robust 2-refinement algorithm in octree or rhombic dodecahedral tree based all-hexahedral mesh generation*, Computer Methods in Applied Mechanics and Engineering, 256 (2013), pp. 88–100.
- [52] Y. ZHANG AND J. QIAN, *Dual contouring for domains with topology ambiguity*, Computer

Methods in Applied Mechanics and Engineering, 217 (2012), pp. 34–45.

- [53] ———, *Resolving topology ambiguity for multiple-material domains*, Computer Methods in Applied Mechanics and Engineering, 247 (2012), pp. 166–178.
- [54] Y. J. ZHANG, *Geometric Modeling and Mesh Generation from Scanned Images*, Chapman & Hall/CRC, Boca Raton, FL, 1st ed., 2016.
- [55] Q. ZHOU AND A. JACOBSON, *Thing10k: A dataset of 10,000 3d-printing models*, 2016.

A Positive Jacobian Check

The supplementary materials include fourteen folders (Case 1 to Case 14). In each folder from Case 1 to Case 11 and Case 13, a Python file `vanilla.ipynb` is provided. These notebooks contain the complete execution records. For each case, the analysis considers all hexes h_j generated by midpoint subdivision in Figure 6 and 25 distinct cells \mathbf{X}_k : the 9 basic 3-refinement cells, plus 15 new cells generated after one local refinement, and 1 additional cell produced after a second local refinement. Also, each cell undergoes all 24 rigid rotations \mathbf{R}_l in the octahedral group. The Jacobian determinant is represented over twelve intersection point parameters $(0, 1)^{12}$ as a Bernstein polynomial $\sum_{\mathbf{0} \leq \mathbf{i} \leq \mathbf{n}} \beta_{\mathbf{i}}(h_j, \mathbf{X}_k, \mathbf{R}_l) B_{\mathbf{i}, \mathbf{n}}(\mathbf{x})$, with coefficients derived via Theorem 5.1, related to the specific hex h_j , the specific cell \mathbf{X}_k , and the rotation \mathbf{R}_l . A positive Jacobian is verified when $\min_{\mathbf{i}}(\beta_{\mathbf{i}}) \geq 0$ and $\max_{\mathbf{i}}(\beta_{\mathbf{i}}) > 0$, ensuring non-negativity across the domain by the convex hull property and preventing all-zero results. As a result, all twelve cases pass the test, validating that the naïve midpoint subdivision scheme guarantees a positive Jacobian for all hexes.

For Case 12, however, applying the same procedure shows that a positive Jacobian cannot be achieved for any cell under any rotation using the naïve midpoint subdivision. To address this, an offset vector $\mathbf{v} = (a, b, c) \in (-1, 1)^3$ is introduced to the barycentric coordinates $(\frac{5+s_1+s_6}{10}, \frac{3+s_{10}+s_{11}}{10}, \frac{4+s_3+s_7}{10})$ of the volume center (refer to Figure 5 for point indices and Table 1 for point coordinates) in one polyhedron. The L-BFGS optimizer from the SciPy package is used to find an offset vector \mathbf{v} such that, for the 10 hex elements h_j in each polyhedron in Case 12 of Figure 6 generated via midpoint subdivision from the 25 cells in the affinely unique maximal set \mathbf{X}_k under 24 rigid rotations \mathbf{R}_l in the octahedral group, all Bernstein coefficients $\beta_{\mathbf{i}}$ of the Jacobian determinant \mathbf{J} are

non-negative. In the whole process, the scenario of all coefficients being zero never happens. Therefore, the optimization problem is to minimize

$$L(\mathbf{v}) = \sum_{j=1}^{10} \sum_{k=1}^{25} \sum_{l=1}^{24} \max \left(0, -\min_{\mathbf{i}} \beta_{\mathbf{i}}(\mathbf{v}, h_j, \mathbf{X}_k, \mathbf{R}_l) \right), \quad (14)$$

where $\mathbf{v} \in (-1, 1)^3$, $\beta_{\mathbf{i}}(\mathbf{v}, h_j, \mathbf{X}_k, \mathbf{R}_l)$ are the Bernstein coefficients of the Jacobian determinant related to the offset \mathbf{v} , the specific hex h_j , the specific cell \mathbf{X}_k , and the rotation \mathbf{R}_l . The goal is to find a \mathbf{v}^* such that $L(\mathbf{v}^*) = 0$, thereby ensuring that $\min_{\mathbf{i}}(\beta_{\mathbf{i}}) \geq 0$ holds true for all configurations. As a result, the code in Case 12 achieves this goal. All the offsets are provided in the `vanilla.ipynb` file.

Due to the rotational symmetry of the two polyhedra in Case 12 with respect to a 180° rotation around the z-axis, it is unnecessary to recompute the offsets for the polyhedron on the opposite side. Instead, the corresponding offsets can be obtained by rotating the cell by 180° around the z-axis, looking up the precomputed offsets $\mathbf{v} = (a, b, c)$, and applying $\mathbf{v}' = (-a, -b, c)$ as the new offsets. Additionally, Case 12 has a mirror symmetry along the x-direction, a case not shown in Figure 6 but illustrated as Case 11 of Figure 1 in (9). Under this mirror transformation, where vertex coordinates are mapped $(x, y, z) \rightarrow (-x, y, z)$, the corresponding offset becomes $\mathbf{v}'' = (-a, b, c)$.

In Case 14, the situation becomes complex. As recorded in its `vanilla.ipynb`, neither the naïve midpoint subdivision nor applying an offset to the volume center $(\frac{5+s_1+s_6+s_9+s_{12}}{12}, \frac{6+s_{10}+s_{11}}{12}, \frac{6+s_7+s_8}{12})$ and solving an optimization problem analogous to Equation 14 (with the only modification being that the number of hex elements j increases from 10 to 24), suffices to guarantee a positive Jacobian in all configurations. While these two approaches succeed in most configurations, the combination of certain cells with certain rotations still result in some negative Bernstein coefficients. Specifically, these problematic cases include rotation configurations 9 and 19 in Case 2; rotation configurations 2 and 13 in Case 5; and rotation configurations 2, 5, 13, and 16 in Case 6 (rotation configuration index can be found in `vanilla.ipynb` files). To resolve this, a piecewise strategy is adopted based on intervals of the intersection point parameters s_7 , s_{11} , and s_{12} . For each interval, the optimization problem in Equation 14 can be solved with its unique offset \mathbf{v}^* . All the intervals and corresponding offsets that ensure positive Jacobians are listed in Table 3. Moreover, note that in the reference implementation, only Case 4-1, Case 7-3, and Case 8-2 are used to resolve

Table 3: Offset vectors for Case 14 across different parameter intervals. The notation “i-j” in the table header denotes configuration i (from 9 basic 3-refinement cells) and rotation j (from 24 rigid rotations in vanilla.ipynb code file).

Intervals s_7, s_{11}, s_{12}	2-9	2-19	5-2	5-13	6-2	6-5	6-13	6-16
(0, 0.05), (0, 0.05), (0, 0.05)	-0.0955 0.0966 0.0237	-0.0955 0.0237 0.0966	-0.0981 0.0602 0.0602	-0.0981 0.0602 0.0602	-0.0258 -0.0165 -0.00727	-0.0258 -0.00727 -0.0165	-0.0258 -0.00727 -0.0165	-0.0258 -0.0165 -0.00727
(0, 0.05), (0, 0.05), [0.05, 1)	-0.0644 0.0601 -0.0141	-0.0644 -0.0141 0.0601	-0.120 0.0853 0.0853	-0.120 0.0853 0.0853	-0.0157 -0.0157 -0.0157	-0.0157 -0.0157 -0.0157	-0.0157 -0.0157 -0.0157	-0.0157 -0.0157 -0.0157
(0, 0.05), [0.05, 0.5), (0, 0.05)	-0.0921 0.0830 0.0265	-0.0919 0.0116 0.105	-0.0933 0.0515 0.0525	-0.0933 0.0515 0.0525	-0.0175 -0.0166 -0.0175	-0.0185 -0.0177 -0.0169	-0.0185 -0.0177 -0.0169	-0.0175 -0.0177 -0.0175
(0, 0.05), [0.5, 1), (0, 0.05)	-0.0302 -0.0250 -0.0262	-0.0919 0.0116 0.105	-0.0933 0.0515 0.0525	-0.0933 0.0515 0.0525	-0.0175 -0.0166 -0.0175	-0.0185 -0.0177 -0.0169	-0.0185 -0.0177 -0.0169	-0.0175 -0.0166 -0.0175
(0, 0.05), [0.05, 1), [0.05, 1)	-0.0557 0.0220 -0.0109	-0.0511 -0.0178 0.0152	-0.0677 0.0149 0.0136	-0.0677 0.0149 0.0136	-0.0186 -0.0186 -0.0186	-0.0174 -0.0174 -0.0174	-0.0174 -0.0174 -0.0174	-0.0186 -0.0186 -0.0186
[0.05, 0.5), (0, 0.05), (0, 0.05)	-0.0919 0.105 0.0116	-0.0921 0.0265 0.0830	-0.0933 0.0525 0.0515	-0.0933 0.0525 0.0515	-0.0185 -0.0169 -0.0177	-0.0175 -0.0166 -0.0166	-0.0175 -0.0175 -0.0166	-0.0185 -0.0169 -0.0177
[0.5, 1), (0, 0.05), (0, 0.05)	-0.0919 0.105 0.0116	-0.0302 -0.0262 -0.0250	-0.0933 0.0525 0.0515	-0.0933 0.0525 0.0515	-0.0185 -0.0169 -0.0177	-0.0175 -0.0175 -0.0166	-0.0175 -0.0175 -0.0166	-0.0185 -0.0169 -0.0177
[0.05, 1), (0, 0.05), [0.05, 1)	-0.0511 0.0152 -0.0178	-0.0557 -0.0109 0.0220	-0.0677 0.0136 0.0149	-0.0677 0.0136 0.0149	-0.0174 -0.0174 -0.0174	-0.0186 -0.0186 -0.0186	-0.0186 -0.0186 -0.0186	-0.0174 -0.0174 -0.0174
[0.05, 1), [0.05, 0.5), (0, 0.05)	-0.0717 0.0471 0.00353	-0.0717 0.00353 0.0471	-0.0886 0.0492 0.0394	-0.0886 0.0492 0.0394	-0.0170 -0.0165 -0.0170	-0.0171 -0.0153 -0.0159	-0.0171 -0.0153 -0.0159	-0.0170 -0.0165 -0.0170
[0.05, 1), [0.5, 1), (0, 0.05)	-0.0717 0.0471 0.00353	-0.0717 0.00353 0.0471	-0.0474 -0.0197 -0.0103	-0.0474 -0.0197 -0.0103	-0.0195 -0.0195 -0.0195	-0.0125 -0.0123 -0.0110	-0.0125 -0.0123 -0.0110	-0.0195 -0.0195 -0.0195
[0.05, 1), [0.05, 1), [0.05, 1)	-0.0483 0.0160 -0.0208	-0.0483 -0.0208 0.0160	-0.0747 0.0210 0.0210	-0.0747 0.0210 0.0210	-0.0206 -0.0206 -0.0206	-0.0206 -0.0206 -0.0206	-0.0206 -0.0206 -0.0206	-0.0206 -0.0206 -0.0206

face ambiguities as a proof of concept, rather than all 17 cases listed in Figure 7. Among these 17 cases, none involves two levels of local refinement, and none of the hexes generated through a single local refinement corresponds to Case 12 or Case 14. Therefore, for Case 12 and Case 14 proofs, only the nine basic 3-refinement cells are considered.

Finally, two additional observations are noted regarding this proof. First, the conclusion that “midpoint subdivision guarantees a positive Jacobian” for Cases 1 to 11 and Case 13 can be extended to the entire parameter space $\xi, \eta, \zeta \in [0, 1]^3$, not only at the eight corner points and the center point. However, extending this proof to Case 12 and Case 14 is challenging. The piecewise offset approach described above has so far failed to establish a full parametric proof. If such a proof can be achieved in the future, it would rigorously ensure that the generated hex elements can be directly applied in engineering simulations. Second, beyond the transition cells shown in Figure 8, a limited number of transition cells from other methods (21, 33, 27) are also examined. However, a complete proof is not feasible due to the high complexity of configurations. The bitter lesson learned here is that the closer the mapping from the unit cube to the transition cell is to an affine transformation, such as when all four points of each face of the transition cell are coplanar, the more tractable the proof becomes. This is why, in the first paragraph of Section 5, it is suggested that the transition cells from (21, 33, 51) are the most promising

candidates for future extensions. For more advanced methods such as (27), it may be necessary to devise more sophisticated midpoint subdivision definitions to enable positive Jacobian guarantees.